HHS Public Access

Author manuscript

Cell. Author manuscript; available in PMC 2019 August 23.

Published in final edited form as:

Cell. 2018 August 23; 174(5): 1247–1263.e15. doi:10.1016/j.cell.2018.07.008.

Hair Cell Mechanotransduction Regulates Spontaneous Activity and Spiral Ganglion Subtype Specification in the Auditory System

Shuohao Sun[#1], **Travis Babola**[#1], **Gabriela Pregernig**[#2], **Kathy So**[2], **Matthew Nguyen**[2], **Michael Su**[2], **Adam Palermo**[2], **Dwight E. Bergles**[1], **Joseph C. Burns**[2,^], and **Ulrich Müller**[1,^,+]

[1]The Solomon Snyder Department of Neuroscience, Johns Hopkins University School of Medicine, 725 N. Wolfe Street, Baltimore, MD 21205, USA

[2]Decibel Therapeutics, 1325 Boylston Street, Suite 500, Boston, MA 02215

[#] These authors contributed equally to this work.

SUMMARY

Type I spiral ganglion neurons (SGNs) transmit sound information from cochlear hair cells to the CNS. Using transcriptome analysis of thousands of single neurons, we demonstrate that murine type I SGNs consist of subclasses that are defined by the expression of subsets of transcription factors, cell adhesion molecules, ion channels and neurotransmitter receptors. Subtype-specification is initiated prior to the onset of hearing during the time period when auditory circuits mature. Gene mutations linked to deafness that disrupt hair cell mechanotransduction or glutamatergic signaling perturb the firing behavior of SGNs prior to hearing onset and disrupt SGN subtype specification. We thus conclude that an intact hair cell mechanotransduction machinery is critical during the pre-hearing period to regulate the firing behavior of SGNs and their segregation into subtypes. Since deafness is frequently caused by defects in hair cells, our findings have significant ramifications for the etiology of hearing loss and its treatment.

INTRODUCTION

Hearing depends on the conversion of mechanical stimuli into electrical signals within the cochlea. The signaling capability of this sensory system is extraordinary, responding to sound-induced vibrations of atomic dimension, amplifying signals >100 fold, and having a large dynamic range that enables us to perceive sound over a broad intensity and frequency

[^]Co-Corresponding Authors Ulrich Müller umuelle3@jhmi.edu, Joseph Burns jburns@decibeltx.com.

[+]Lead contact, Ulrich Müller, Solomon Snyder Department of Neuroscience, Johns Hopkins Medical Institute, 725 N. Wolfe Street, Baltimore, MD 21209, USA, P:443–287-4762, umuelle3@jhmi.edu

AUTHOR CONTRIBUTION

All authors contributed to experimental design and data analysis. RNA-Seq and data analysis were carried out by GP, AP, KS, MS and JB. Analysis of mice by histology was carried out by SS. MN contributed RNAscope data. Spontaneous activity was evaluated by TB and DB. UM, JB, SS and GP wrote the manuscript with input from all authors.

DECLARATION OF INTERESTS

JB, MS, AP, GP, MN and KS are employees of Decibel Therapeutics. UM is a co-founder of Decibel Therapeutics and a member of its scientific advisory board.

DATA AND SOFTWARE AVAILABILITY

All software tools can be found online (see Key Resource Table). Raw data files have been uploaded to GEO: GSE114759

range. The mechano-electrical conversion critical for hearing is carried out by hair cells (Fig. 1A). Three rows of outer hair cells (OHCs) amplify sound-induced vibrations that reach the cochlea. These vibrations induce deflection of stereocilia at the apical surface of inner hair cells (IHCs) (Fig. 1A), open transduction channels in stereocilia, and lead to excitation of spiral ganglion neurons (SGNs). Sound frequencies are relayed to the nervous system as a tonotopic map, with IHCs at the base of the cochlea responding to the highest frequencies and those at the apex to the lowest frequencies (Gillespie and Muller, 2009; Meyer and Moser, 2010).

IHCs and OHCs are innervated by SGNs, but with distinct synaptic organization. Type I SGNs exhibit input from only one IHC, whereas type II SGNs extend long projections and receive input from dozens of OHCs. Although IHCs exhibit one-to-one coupling with SGNs, each IHC is innervated mono-synaptically by 5 – 30 type I SGNs that transmit sound information to the CNS. Type I SGNs constitute 95% of all SGNs while the remaining 5% are the type II SGNs (Fig. 1A) (Perkins and Morest, 1975; Ryugo, 1992; Spoendlin, 1973). Type II SGNs are not essential for transmission of sound information to the CNS and instead appear to have a role in damage perception and pain signaling (Flores et al., 2015; Liu et al., 2015). Like hair cells, type I SGNs are organized tonotopically and each SGN is most sensitive to one particular frequency, coinciding with its relative position along the cochlear partition (Davis and Crozier, 2015; Meyer and Moser, 2010). However, not all properties of SGNs vary tonotopically. The most sensitive region for hearing is in the middle part of the cochlea, while neurons in the apical and basal region are less sensitive (Heffner et al., 1994; Koay et al., 2002; Ruggero and Temchin, 2002).

In addition to this regional specificity, type I SGNs that innervate single IHCs also exhibit diverse characteristics (Heil and Peterson, 2015). Type I SGNs have variable spontaneous rates (SRs) that are inversely correlated with their threshold to sound and dynamic range (Liberman, 1978; Sachs and Abbas, 1974). Discharge rates from near 0 to 120 spikes per second have been observed. The distribution of SGNs with different SRs is largely bimodal with a peak at low rates (≤ 1 spike/sec) and higher rates (60–70 spikes/sec) in some species such as cats but not in rodents where nerve fibers show a gradual increase from low to high SRs (Heil and Peterson, 2015). Based on studies in cats, a classification of SGNs into three classes has been proposed: high-SR (>18 spikes/s), medium-SR (0.5–18 spikes/s), and low-SR (<0.5 spikes/s) fibers. This classification takes into account SRs and relative thresholds for activation by sensory input (Liberman, 1978a). In cats, low- and high-SR fibers preferentially contact the modiolar and pillar sides of IHCs, respectively (Liberman, 1982). In rodents single IHCs also appear to be innervated by fibers with different SRs (Liberman et al., 2011; Wu et al., 2016). This is compelling because it could allow for parallel information processing by functionally distinct neurons that receive input from a single hair cell.

Here we analyzed molecular diversity within murine SGNs. Using massive parallel single-cell RNA sequencing (scRNA-Seq) we demonstrate that type I SGNs are molecularly diverse and are comprised of three main subtypes, which can be subdivided into six classes. These molecularly distinct subtypes reach maturity postnatally when auditory circuits mature. Disruption of mechanotransduction or glutamate release by hair cells affect the

spontaneous activity and subtype specification of SGNs prior to hearing onset, suggesting that activity patterns experienced by SGNs during this critical period influence their developmental trajectories. Our analysis of the molecular diversity of SGNs leads to the surprising conclusion that an intact mechanotransduction machinery is critical even in the pre-hearing period to promote spontaneous activity and molecular diversification of type I SGNs.

RESULTS

Identification of SGN subtypes by single-cell RNA-Sequencing

To molecularly profile SGNs, we carried out massively parallel scRNA-Seq experiments with cells obtained from the inner ears of nine weeks-old, male CBA/CaJ mice. We optimized the micro-dissection procedure to enrich for sensory neurons (see STAR Methods) and independently dissociated cells from four mice for use in droplet microfluidics (10X Genomics Chromium) to obtain cell-barcoded cDNAs that were sequenced. After filtering out low complexity droplets, the dataset consisted of 17,556 high quality cells (Fig. S1, Table S1) (Macosko et al., 2015; Zheng et al., 2017).

Mature type I SGNs can be distinguished from type II SGNs by high levels of *Tubb3* expression while mature type II SGNs strongly express *Prph* (Barclay et al., 2011; Hafidi, 1998; Lallemend et al., 2007; Mou et al., 1998; Nishimura et al., 2017; Vyas et al., 2017). Unbiased clustering revealed groups of neurons that were separable on a t-Distributed Stochastic Neighbor Embedding (t-SNE) plot of all cells (Fig. 1B). Based on expression of *Tubb3* and *Prph*, three of the clusters represented putative type I SGNs (red cells), and one cluster putative type II SGNs (grey cells) (Fig. 1B; Fig. S2A,C). SGNs comprised 40% (6,713) of the total cell number, confirming that our micro-dissection enriched these neurons. The remaining cells consisted of at least 20 additional clusters (Fig. 1B; Fig. S2A-B, S3).

While the identity calling of putative SGNs was robust to a number of clustering parameter variations (Fig. S4), non-neuronal cell types in the dataset could introduce biases into neuronal sub-clusters. Therefore, we selected the four putative groups of neurons and re-clustered the data in the absence of other cell types. After filtering out cells with undetermined identity (8%, Fig. S5), 6,113 SGNs remained (see STAR Methods). In agreement with the expected relative contribution of the two types of neurons to the SGN pool (Perkins and Morest, 1975; Ryugo, 1992; Spoendlin, 1973), 98% and 2% of SGNs were assigned to the type I and type II identity, respectively.

1,616 genes were differentially expressed between type I and type II SGNs (absolute log fold-change > 0.1; adjusted p-value < 0.01; Table S2). Top hits that were elevated in type II SGNs included known markers such as *Prph, Gata3*, *Mafb*, and *Th* (Barclay et al., 2011; Hafidi, 1998; Lallemend et al., 2007; Mou et al., 1998; Nishimura et al., 2017; Vyas et al., 2017). Genes that were significantly increased in type I SGNs included structural proteins (*Tubb3, Nefl*) and ion channels (*Kcnc3* and *Scn4b*) (Fig. 1C).

Three subtypes of type I SGNs can be distinguished in cats based on spontaneous rates of firing and sound detection thresholds (Liberman, 1978b). We re-analyzed the putative type I SGNs, varying parameters to extract three clusters from the dataset that we named IA, IB, and IC (Fig. 1D, Figs. S5, S6, S7). Cluster IA contained 39% of the cells, cluster IB 27%, and cluster IC 34%. Cluster separation was driven by a host of genes and was reproducible across all four mice from which cells were obtained (Fig. 1E,F; Fig. S7A,B,F; Table S3). Most of the identified genes have not been shown to be expressed in subsets of SGNs. An exception is *Pou4f1*, which is confined to a subset of SGNs (Xiang et al., 1997).

A subset of the sequenced type I SGNs expressed significant levels of glial genes (Fig. S6B). This was unsurprising, given that type I SGNs are myelinated. Glial fragments likely remained attached to the SGNs after dissociation. When we restricted our analysis to pure type I SGNs with very low expression levels of glial genes (clusters 4 and 5; Fig. S6C,D), we recapitulated all of our main findings (Fig S6E,F,G; Tables S4,S5). We also carried out differential expression analysis between purer SGNs and contaminated SGNs. Only a small percentage of genes differentially expressed between the subtypes corresponded to “contaminating genes” (Fig. S6H).

While our data analysis was guided by reported electrophysiology findings, we explored whether there was additional SGN diversity. An alternative clustering procedure based on independent component analysis (ICA) and different parameters (see STAR Methods) split the cells into six clusters. This analysis revealed a set of genes that was expressed in a subset of cells from each of the previously identified groups (Fig. S7).

Verification of SGN subtypes

To verify RNA profiling data, we analyzed the expression of putative markers for the type I SGNs subtypes defined by transcriptome analysis (Fig. 1D-F) by immunohistochemistry.TuJ1 distinguishes type I SGNs from type II SGNs (Barclay et al., 2011; Lallemend et al., 2007) and we identified NGFR as a type II SGN marker (Fig. 1C). Immunostaining of histological sections at P28 revealed expression of TuJ1 in the majority of SGNs, with the exception of a smaller neuronal population at the periphery of the ganglion where type II SGNs tend to be localized (Fig. 2A). These neurons at the periphery expressed high levels of NGFR (Fig. 2A). Staining of whole mounts demonstrated that $NGFR^+$ cells extended projections to OHCs, as predicted for type II SGNs (Fig. 2B).

Next, sections were co-stained with antibodies to TuJ1 to identify type I SGNs and with antibodies to CALB2 (type IA), CALB1 (type IB), and POU4F1 (type IC). As predicted high levels of CALB2, CALB1 and POU4F1 were expressed in subsets of SGNs (Fig. 1C; 52 ± 2 % $CALB2^+$; 26 ± 1 % $CALB1^+$; 27 ±1% $POU4F1^+$) (Fig. 2D). Double-immunfluorescence experiments confirmed that CALB2, CALB1, and POU4F1 (Fig. 2E) labeled distinct SGN populations, with a small overlap between populations (Fig. 2E,F).

We confirmed by RNAscope that *Lypd1* (type IC marker) was present in a subset of SGNs (Fig. 2G), and that *Calb2* and *Pou4f1* were expressed in different SGN subpopulations (Fig. 2E; 50 ± 3 % *Pou4f1*$^+$, 32 ± 2 % *Calb2*$^+$; overlap 4 ± 1%) in good agreement with the values obtained by immunohistochemistry (Fig. 2F).

Contrasting expression patterns of gene families in SGN subtypes

Neuronal subtypes in the cortex can be distinguished by the differential expression of members of gene families belonging to six categories (Table S6): (1) transcription factors (TFs); (2) cell-adhesion molecules (CAMs); (3) receptors for neurotransmitters and modulators; (4) voltage-gated ion channels; (5) regulatory signaling proteins; and (6) neuropeptides and vesicle release machinery (Paul et al., 2017). We identified genes that were differentially expressed between subtypes for each class (Fig. 3A; Fig. S7B; Table S3). Fig. 3B shows violin plots for some of the genes, highlighting that while differences in gene expression were prominent between type IA, IB and IC SGNs, they were not all-or-none. Differences in the expression of CAMs, cell signaling molecules, ion channels and neurotransmitter receptors (Fig. 3A), may reflect differences in the innervation pattern of IHCs by subtypes of SGNs and differences in synaptic connectivity within the auditory nucleus. For example, *Grm8*, which encodes a metabotropic glutamate receptor, was highly expressed in type IC SGNs, but not in type IA and IB SGNs.

Innervation of inner hair cells by type I SGNs

In cats, high-SR neurons have an increased mitochondrial content and increased fiber thickness compared to low-SR and medium-SR fibers (Liberman, 1980; Merchan-Perez and Liberman, 1996). Low-, and high-SR fibers in cats also preferentially contacted the modiolar and pillar sides of IHCs, respectively (Liberman, 1982). In mice, SRs of type I SGNs also vary (Taberner and Liberman, 2005; Wu et al., 2016) and synaptic contacts at the modiolar and pillar side of IHCs show structural differences (Liberman et al., 2011). Intriguingly, type IA SGNs had elevated expression levels of genes associated with mitochondrial function compared to type IB and IC SGNs (Fig. 3C) indicative of increased mitochondrial content. Type IA SGNs also expressed higher levels of neurofilament transcripts (Fig. 3D), which correlates with an increased axonal diameter (Elder et al., 1998; Hoffman et al., 1987; Marszalek et al., 1996; Xu et al., 1996). Thus, type IA SGNs most closely correspond to high-SR fibers.

We also traced projections to IHCs. Cochlear whole mounts were immunostained for CALB2 and TuJ1, which are detectable in projections of type I SGNs (Fig. 3E). CALB2 also labels IHCs (Fig. 2B), thus allowing us to identify targets of type I SGNs. We collected serial optical sections through the sensory epithelium and generated 3D projections of 65 hair cells. The type I SGN marker $TuJ1^+$ labeled all nerve fibers contacting the basal part of IHCs at the modiolar, medial and pillar side (Fig. 3E,F). $CALB2^+$ type IA SGN projections were prominent on the pillar side of IHCs, with some projections innervating the medial side (Fig. 3E,F). Our CALB1 antibody occasionally revealed CALB1 expression in nerve fibers innervating IHCs. $CALB1^+$ fibers segregated from $CALB2^+$ fibers and projected to the modiolar side of IHCs (Fig. 3F). These findings indicate that type I SGN subtypes converge on single IHCs with distinct innervation patterns.

Subclasses of SGNs are specified postnatally

We next asked whether molecular differences in type I SGNs were observed at the progenitor level or were detectable only subsequently within the maturing ganglion. SGNs in mice are born from progenitors in the otic vesicle and delaminate around embryonic day

(E) 10 to form the spiral ganglion (Fig. 4A). Postmitotic SGNs elaborate projections to hair cells by P0 and refine them during the first few postnatal weeks (Echteler, 1992; Huang et al., 2012; Huang et al., 2007; Koundakjian et al., 2007; Perkins and Morest, 1975; Simmons, 1994; Sobkowicz et al., 1986). Mechanotransduction currents in mouse hair cells are detected at birth and reach mature levels in 5 −10 days (Kim and Fettiplace, 2013; Lelli et al., 2009; Pan et al., 2013). The onset of hearing in mice does not occur until P12-P14 (Ehret, 1983; Mikaelian and Ruben, 1965) and synapse formation between SGNs and hair cells progresses up to P28 (Fig. 4A) (Huang et al., 2012; Liberman and Liberman, 2016; Sobkowicz et al., 1986). We therefore immunostained sections of the inner ear between P0 and P28 with markers for SGN subtypes

NGFR, CALB2, CALB1, and POU4F1 were expressed in essentially all SGNs at P0 (Fig. 4B,C) but their expression was gradually refined at subsequent ages (Fig. 4C). Type I SGNs could be distinguished from type II SGNs between P0-P7 (Fig. 4B,C), but segregation of type I SGN markers continued up to P28 (Fig. 4B,C). While we cannot exclude molecular differences between SGNs in prenatal animals, postmitotic SGNs undergo a major refinement in molecular phenotype in the first few postnatal weeks.

Specification of SGNs is affected by mutations that block mechanotransduction channels

Spontaneous and sensory input driven activity promotes their maturation and connectivity of neuronal circuits. The test whether activity dependent mechanisms influence the specification of subtypes of SGNs, we analyzed mice with mutations in genes encoding components of the mechanotransduction machinery of hair cells. Mechanotransduction in hair cells depends on tip links and an associated ion channel complex containing LHFPL5, TMIE and TMC1/2 (Fig. 5A) (Zhao and Muller, 2015). Mutations in *Tmie* and the tip-link component *Pcdh15* abolish transduction (Alagramam et al., 2011; Zhao et al., 2014), while *Lhfpl5* mutations reduce transduction by ~90% (Xiong et al., 2012). Histological sections were prepared from mice carrying mutations in *Pcdh15*, *Lhfpl5* and *Tmie* between P0 - P28 and analyzed for the expression of SGN subtype markers. Quantification of total SGN numbers at P28 revealed no difference between wild-type and mutants, suggesting that SGN survival was not affected by the mutations under study up to P28 (Fig. 5D). In mice deficient in *Pcdh15* and *Tmie,* adding the percentage of $TuJ1^+$ neurons expressing CALB2, CALB1, or POU4F1 gave values well over 100% (Fig. 5B,C), suggesting that specification of type IA, IB and IC SGN subtypes was affected, resulting in co-expression of markers that typically define type I SGN subtypes. Expression of subtype markers was affected less severely in *Lhfpl5* mutants (Fig. 5C,D), consistent with the reduction, but not elimination, of mechanotransduction currents in *Lhfpl5* mutants (Xiong et al., 2012). Co-immunolocalization studies with antibodies that mark type IA, IB and IC SGNs in mice with mutations in *Pcdh15* and *Tmie* confirmed a large increase in the number of neurons co-expressing markers for type IA, IB and IC SGNs (Fig. 5E).

Analysis of the expression of TuJ1 (type I SGNs) and NGFR (Type II SGNs) revealed a 2–4 fold increase in the percentage of $NGFR^+$ SGNs in *Pcdh15*, *Tmie* and *Lhfpl5* mutants (Fig. 5F,G). Less than 5% of NGFR expressing SGNs co-express TuJ1 in wild-type mice, while in *Pcdh15*, *Tmie* and *Lhfpl5* mutant mice the number was increased by 4–10 fold (Fig. 5F,G).

These findings suggest that disruption of mechanotransduction in IHCs and OHCs impairs proper segregation of type I and type II SGNs, as well as specification of type I SGNs into subclasses. Analysis of the developmental time course in *Tmie-ko* mice confirmed that defects in the segregation of molecular markers that identify SGN subtypes were apparent at hearing onset (P14; Fig. 5H). We conclude that functional mechanotransduction is important for SGN specification at stages prior to hearing onset.

Specification of SGNs is disrupted by mutations that block glutamatergic signaling

Glutamatergic synaptic communication between IHCs and type I SGNs depends on the glutmate transporter VGLUT3 (Fig. 6A) (Ruel et al., 2008; Seal et al., 2008). Glutamate release from hair cells prior to hearing onset is also involved in generating spontaneous activity in the developing auditory system (Tritsch et al., 2007; Wang et al., 2015). If activity dependent processes participate in SGN specification, then disruption of this transporter should affect SGN development. Analysis of sections from *Vglut3* knock-out (*Vglut3-ko*) mice (Seal et al., 2008) demonstrated that the expression pattern of SGN subtype markers was strikingly altered in the mutants, but in patterns that differed from mice with defects in mechanotransduction. The percentage of $CALB1^+$ and $CALB2^+$ neurons was increased in *Vglut3-ko* mice, and the percentage of $POU4F1^+$ neurons was reduced (Fig. 6A-C). Total numbers of SGNs were also decrease at P28 in *Vglut3-ko* mice, although they were not different between wild-type and mutants at birth (Fig. 6D). Since SGNs are postmitotic at birth, these findings suggest that some neurons in *Vglut3-ko* mice had died postnatally.

We also observed in *Vglut3-ko* mice a large increase in the number of neurons co-expressing markers for type IA, IB and IC SGNs (Fig. 6E), as well as markers for type I and type II SGNs. The defects in subtype specification were detectable in *Vglut3-ko* mice at P14 (Fig. 6H), providing evidence that they were established in the pre-hearing period. These data suggest that in the absence of glutamatergic signaling, molecular and functional diversification between subtypes of type I SGNs and between type I and type II SGNs was affected.

SGNs exhibit altered patterns of activity in *Tmie-ko* and *Vglut3-ko* mice

SGNs fire discrete bursts of action potentials prior to hearing onset, due to periodic depolarization of IHCs by K^+ released from inner supporting cells (ISCs; Fig. 7A,B) (Tritsch et al., 2007; Wang et al., 2015). To determine if loss of *Tmie* or *Vglut3* alters the SGN activity during this period, we examined the firing behavior of SGNs in cochlear whole-mounts at P5–7. Juxtacellular recordings (Fig. 7A) revealed that SGNs in *Tmie-ko* mice continued to exhibit spontaneous activity, with action potentials grouped into bursts (Fig. 7B, C), but had lower activity rates than controls (Fig. 7D, E), with lower average frequencies of individual action potentials and bursts (Fig. 7F). Burst duration and number of action potentials per burst also trended lower in *Tmie-ko* mice but did not reach significance (Fig. 7F), while the timing of action potentials within bursts was similar between *Tmie-ko* and controls (Fig. 7G) (Sonntag et al., 2009; Tritsch et al., 2010). However, there were fewer short interspike intervals (5–10 ms) in SGNs from *Tmie*-ko mice. These short intervals occur because each IHC Ca^{2+} spike typically triggers multiple action potentials with short intervals (i.e. a mini-burst) (Sonntag et al., 2009; Tritsch et al., 2010).

This reduction in action potentials per mini-burst suggests that SGNs in *Tmie-ko* mice are less excitable than controls or that IHCs release less glutamate in response to each Ca^{2+} spike, thus leading to changes in the pattern of spontaneous activity. Application of the mechanotransduction channel inhibitor d-tubocurarine (d-TC, 50 μM) reduced the frequency and duration of bursts, as well as the average spike frequency (Fig. 7F), mimicking patterns of activity observed in *Tmie-ko* mice, indicating that these changes in activity primarily reflect the contribution of mechanotransduction channels.

Postsynaptic AMPA receptor-meditated currents are absent in *Vglut3-ko* mice (Seal et al., 2008). As glutamatergic transmission is required for excitation of SGNs prior to hearing onset (Tritsch et al., 2007; Zhang-Hooks et al., 2016), we predicted that SGNs should not exhibit periodic bursts of action potentials in *Vglut3-ko* mice. Unexpectedly, juxtacellular recordings revealed that SGNs continued to exhibit spontaneous firing in *Vglut3-ko* mice (Fig. 7I). SGN bursts were less distinct in *Vglut3-ko* mice than in controls (Fig. 7H-K), and although bursts were longer they contained fewer spikes (Fig. 7J). Mini-bursts were also absent in *Vglut3-ko* mice (Fig. 7K), as expected if IHC Ca^{2+} spikes are no longer responsible for inducing SGN firing (Tritsch et al., 2010). Thus, loss of IHC-SGN synaptic communication does not abolish periodic burst firing of SGNs prior to hearing onset but induces distinct activity patterns. We conclude that genetic disruption of two IHC genes involved in sensory transduction, *Tmie* and *Vglut3*, lead to distinct changes in the activity and molecular specification of SGNs prior to hearing onset, suggesting that the firing pattern exhibited by SGNs during this period plays a crucial role in guiding the maturation of the auditory system.

DISCUSSION

We provide here a comprehensive characterization of the gene expression program of SGNs, identify molecularly distinct SGN subtype and demonstrate that activity dependent mechanisms are critical for SGN subtype specification. Previous studies had identified several genes that are expressed at different levels in mature type I and type II SGNs (Barclay et al., 2011; Hafidi, 1998; Lallemend et al., 2007; Mou et al., 1998; Nishimura et al., 2017; Vyas et al., 2017), and we have identified here many more. The functional consequences of these differences need to be explored, but one gene, *Ngfr*, provides an interesting example. *Ngfr* is highly expressed in type II SGNs. *Ngfr* encodes the low affinity p75 neurotrophin receptor, which also interacts with tropomyosin kinase (Trk) receptors to modulate ligand binding to these high affinity neurotrophin receptors (Huang and Reichardt, 2003). Neurotrophins regulate cochlear innervation by type I SGNs via Trks (Fritzsch et al., 1997), but the role of p75 in the inner ear is less clear. p75 when expressed in the absence of Trks can activate cell death pathways (Lu et al., 2005) and p75 is upregulated in the inner ear in response to injury (Tan and Shepherd 2006). The difference in p75 expression might indicate differences in the response of type I and type II SGNs to neurotrophins.

Our findings reveal differences in the expression of a wide range of genes in type I SGNs suggesting that these neurons are functionally diverse and consisting of three major subtypes. These subtypes were also identified in a parallel study (Shrestha et al.; this issue of Cell) and might correspond to the three functional subtypes of type I SGNs proposed by

Liberman (1978) based on electrophysiological criteria and threshold of activation to sound. Type IA neurons most closely resemble high-SR fibers in cats, a conclusion that was also reached by the Goodrich laboratory (Shrestha et al.; this issue of Cell). Like high-SR fibers, type IA neurons innervate IHCs on the pillar side and express elevated levels of mitochondrial genes and neurofilament genes indicative of increase mitochondrial content and axonal diameter.

When we applied alternative clustering methods to our data, we identified six subtypes of type I SGNs, suggesting greater diversity in this neuronal population than previously anticipated. Even in species where neurons have been grouped according to SR rates, SR rates vary even within groups (Heil and Peterson, 2015). Furthermore, type I SGNs are organized tonotopically and neurons innervating the middle part of the murine cochlea show the lowest thresholds of activation by sound and highest resting membrane potentials (Liu and Davis, 2007; Liu et al., 2014). Thus, some of the observed molecular differences might reflect additional differences in the physiological properties of SGNs.

Our findings suggest that activity dependent mechanisms are critical for the diversification of SGNs. Action potentials that occur independent of external input have been observed in the nervous system and they affect both cell proliferation and differentiation (Arroyo and Feller, 2016; Cohen-Cory, 2002; Huberman et al., 2008; Kandler, 2004; Wang and Bergles, 2015). In the auditory system, brain stem circuitry shows sensory-input independent activity coincident with structural and functional maturation (Kandler et al., 2009; Kandler and Gillespie, 2005; Tritsch and Bergles, 2010; Tritsch et al., 2007; Wang et al., 2015). Despite the immaturity of ribbon synapses at early postnatal stages, IHCs excite SGNs through activation of their glutamate receptors (Beutner and Moser, 2001; Glowatzki and Fuchs, 2002; Johnson et al., 2005; Robertson and Paki, 2002; Tritsch and Bergles, 2010; Wang and Bergles, 2015). Inner supporting cells are implicated in the generation of spontaneous activity in the cochlea (Tritsch et al., 2007; Wang et al., 2015), but the involvement of IHC in this process are less well understood.

Our findings show that active mechanotransduction channels in hair cells are critical for shaping spontaneous firing patterns in SGNs before hearing onset. Previous studies have shown that spontaneous release of ATP initiates IHC excitation at early postnatal ages to induce glutamate release from IHCs. ATP release induces crenations in supporting cells surrounding hair cells (Tritsch et al., 2007). These crenations could provide a mechanical stimulus to hair cells leading to the activation of mechanotransduction channels in the prehearing period, amplifying the direct depolarization of SGNs produced by K^+ release from inner supporting cells.

Perturbations of mechanotransduction channels and glutamate release affected the spontaneous activity of SGNs and their subtype specification, suggesting that the two events are linked. Consistent with this model, subtype specification of SGNs was initiated in the pre-hearing period coincident with the time-frame when spontaneous activity in SGNs. Refinement of SGN subtypes continues into the fourth week after birth, thus extending into the time of active hearing, suggesting that sensory input driven events also participate in SGN specification. Maturation of ribbon synapses continues until the fourth postnatal week

(Huang et al., 2012; Liberman and Liberman, 2016; Sobkowicz et al., 1986). This time-frame also overlaps with the period when murine SGNs refine their firing properties from an immature state to a range of fibers differing in their SRs (Wu et al., 2016), indicating an intriguing interplay between molecular and functional diversification.

Disruption of mechanotransduction in IHCs and OHCs and glutamate release from IHCs affected spontaneous activity patterns and SGN subtype specification in distinct ways. In the absence of mechanotransduction, bursts of action potentials are reduced. Neurons do not die (at least up to P28), but increased numbers of SGNs continue to co-express markers for subtypes of type I SGNs suggesting that they remain immature. In contrast, inactivation of *Vglut3* changed the pattern of spontaneous activity to longer bursts with fewer spikes, altered SGN subtype specification and caused loss predominantly of one type I SGNs subtype. How can the differences be explained? Glutamate release may regulate SGN survival and glutamate may still be released from hair cells even in the absence of mechanotransduction channels, but not when VGLUT3 is absent. Other mechanisms might also be at play. Notably, inactivation of *Vglut3* affects IHCs, while mutations in *Pcdh15*, *Tmie* and *Lhfpl5* affect both IHCs and OHCs. In each instance, increased numbers of neurons co-express type I and type II markers suggesting that the maturation of both principal SGN subtypes is affected. During development, nerve fibers of type II SGNs bypass IHCs while type I SGNs innervate IHCs. SGNs elaborate excessive branches that are subsequently refined (Echteler, 1992; Huang et al., 2012; Huang et al., 2007; Koundakjian et al., 2007; Perkins and Morest, 1975; Simmons, 1994; Sobkowicz et al., 1986). This refinement process is perhaps dependent on activity-dependent mechanisms.

Hearing loss is the most common form of sensory impairment in humans. More than 70 genes have been linked to the disease and mutations in many genes disrupt hair cell function (Dror and Avraham, 2010; Richardson et al., 2011). Our findings predict that hair cell defects will secondarily affect the development of auditory circuitry. Significantly, hearing loss can also be caused by loss of synaptic innervation of IHCs by SGNs (Liberman, 2017). Low-SR synapses seem to be particularly vulnerable to noise or ageing (Furman et al., 2013; Schmiedt et al., 1996). Recent findings suggest that the type IC neurons are lost in ageing mice (Shrestha et al.; this issue of Cell), lending further support to the notion that they might correspond to low-SR fibers. It will be important to determine in more detail the extent to which the specific SGN subtypes are affected by noise and ageing, and whether IHC activity at adult ages is required to maintain the proper distribution of type I SGN subtypes.

STAR METHODS

Lead contact Ulrich Müller Solomon Snyder Department of Neuroscience Johns Hopkins Medical Institute 725 N. Wolfe Street, Baltimore, MD 21209, USA P:443–287-4762 umuelle3@jhmi.edu

CONTACT FOR REAGENT AND RESOURCE SHARING

Requests for resources and reagents should be directed to Lead Contact Ulrich Mueller (umuelle3@jhmi.edu)

EXPERIMENTAL MODEL AND SUBJECT DETAILS

Ethic statement

IACUC Institutional Review Boards at the Johns Hopkins University School of Medicine approved all animal procedures.

Mouse strains

Tmie-ko, *Lhfpl5-ko*, *Vglut3-ko,* and *Pcdh15-av3j* mice were maintained on a C57BL/6 background and have been described previously (Alagramam et al., 2011; Borgius et al., 2010; Madisen et al., 2010; Seal et al., 2008; Xiong et al., 2012; Zhao et al., 2014).

METHOD DETAILS

Cell dissociation of SGNs for single-cell RNA-Seq

Temporal bones from 9 wko, male CBA/CaJ mice (n = 8 capsules from 4 mice) were isolated in ice-cold Leibovitz's L-15 medium, and the overlying bone and lateral wall was extracted from apex to base, leaving just the modiolus. The remaining structures consisted of the spiral ganglion, the spiral limbus, inner sulcus, and portions of the organ of Corti and outer sulcus. Microdissected tissue from each mouse was pooled in a solution of Leibovitz containing 200 units/mL collagenase IV (Sigma) and 10 kunitz/ml DNase I (Stem Cell Technologies) and incubated for 30 min at 37 °C to digest extracellular matrix. The collagenase IV solution was then replaced with EBSS containing 20 units of papain (Worthington Biochemical), 1 mM L-cysteine, 0.5 mM EDTA, 15 mM HEPES, and 10 kunitz/ml DNase I and incubated for an additional 30 min at 37 °C, triturating with a 1000 μL pipette every 10 min to generate a single cell suspension. An equal volume of Leibovitz containing 20% ovomucoid protease inhibitor (Worthington Biochemical) was added, and the dissociated cells were passed through a 20 μm filter (pluriSelect) to remove large debris. The cells were pelleted at 300g for 5 min, washed twice with PBS containing 0.04% BSA, and then pelleted and resuspended in PBS/BSA solution. Finally, a 9 μL sample of the cell suspension was counted on a Luna Fl automated counter using an AO/PI cell viability assay (Logos Biosystems). Total time from euthanasia to single-cell capture was ~3 h.

Single-cell capture, library preparation, and RNA-Seq

The cell suspension was diluted to a concentration of ~500 cells per μL and immediately captured, lysed, and primed for reverse transcription (RT) using the high throughput, droplet microfluidics Gemcode platform from 10X Genomics with v2 chemistry (Zheng et al., 2017). Each droplet on the Gemcode co-encapsulates a cell and a gel bead that is hybridized with oligo(dT) primers encoding a unique cell barcode and unique molecular identifiers (UMIs) in lysis buffer. The capture process takes 6 min, after which the transcriptomes captured on gel beads are pooled and immediately reverse transcribed to cDNA. Since all cDNA is pooled and PCR amplified, cell barcodes and UMIs facilitate demultiplexing of the originating cell and mRNA transcript after sequencing. RT-PCR amplification of cDNA, and preparation of a library from 3' ends were conducted according to the manufacturer's published protocol. We performed 14 cycles of PCR amplification of cDNA. The library was

sequenced on an Illumina NovaSeq 6000 with an S2 100 cycle reagent kit at the Broad Institute Sequencing Facility.

Processing and QC of single-cell RNA-Seq data

Reads were demultiplexed, aligned to the GRCm38 mm10 assembly reference genome, and filtered; and cell barcodes and UMIs were quantified using the 10X Genomics Cell Ranger pipeline with default parameters (https://support.10xgenomics.com/single-cell-gene-expression/software/overview/welcome). Cell Ranger uses STAR (Dobin et al., 2013) for alignment and manufacturer's software for all other steps (Zheng et al., 2017). For each gene, UMI counts of all transcript isoforms are summed to obtain a digital measure of total gene expression. Droplets containing cells are selected from empty droplets based on ranked UMI complexity of the cell barcodes. Processing the single-cell data from all four mice with the Cell Ranger pipeline resulted in a digital expression matrix of 27,998 genes by 17,900 cells.

All further filtering and downstream analysis of single-cell data described in subsequent sections was performed with Seurat v2.1, using default parameters unless specified (http://satijalab.org/seurat/) (Butler et al., 2018; Satija et al., 2015). To limit the influence of low complexity cells and genes, cells with fewer than 100 expressed genes (i.e. transcript count > 1), and genes with detectable expression in 10 or fewer cells were removed. This did not remove any cells from the original matrix, but it reduced the number of genes to 18,143.

Red blood cell contamination is a concern when dissociating cells from the adult cochlea since there is a large niche of erythroid cells near the bony apex. Red blood cells are highly enriched for hemoglobin transcripts, and hemoglobin protein occupies up to 98% of the red blood cell cytosol (D'Alessandro et al., 2010). Therefore, we analyzed the fraction of total transcript counts from each single cell that were comprised of transcripts from the hemoglobin genes (*Hba-a1*, *Hba-a2*, *Hbb-bh1*, *Hbb-bs*, *Hbb-bt*). Relatively few cells (<2%) showed substantial levels of contamination (Fig. S1A). Nevertheless, we removed any cell with >5% contamination, which reduced the total number of cells to 17,556.

The resultant data was of comparable quality and complexity as other published droplet-based single-cell resources (Macosko et al., 2015; Zheng et al., 2017). QC metrics for sequencing, alignment, and quantification are listed for each mouse in Table S1. Per cell, there were 134,912 ± 46,895 mean reads, 5,251 ± 1,256 median UMIs, 2,142 ± 396 median genes. At this sequencing depth, UMI complexity reached 83 ± 3% saturation, which is well into the linear plateau of the saturation curve. Fig. S1 shows plots of UMI and gene complexity categorized by mouse and cluster (as defined in Fig. S2A). Of note, UMI and gene complexity were noticeably bimodal (Fig. S1B). A comparison of the number of UMIs and genes per cell for SGNs versus all other cell types revealed that much of the bimodality was driven by higher complexity of neurons (Fig. S1D). The median number of genes per SGN was 4,202. Higher complexity of transcript species is expected for differentiated cells like neurons (Zeisel et al., 2015).

Dimensionality reduction and clustering

Full descriptions of Seurat's clustering procedure can be found at http://satijalab.org/seurat/. Briefly, after QC and filtering, gene expression for each cell was normalized by total transcript count, multiplied by a factor of 10,000, and log-transformed. To identify highly variable genes that account for cellular heterogeneity, genes were binned by average expression level and selected based on the z-score of their dispersion within each bin. For unbiased clustering of cells, Seurat uses a modularity-based method on shared nearest neighbor graphs, which are constructed from the Euclidean distances of reduced dimensionality space. Modularity optimization is then applied to cluster the cells, with the degree of clustering controlled by a user-defined resolution parameter. Principal component analysis (PCA) was used for dimensionality reduction and was calculated from z-scored residuals of the regressed gene expression matrix. We regressed on sample (mouse) and the number of UMIs per cell to control for unwanted variation across samples and sequencing depth. PCA was first computed for the highly variable genes then projected onto the entire matrix. For all clustering analyses, we chose twice the number of PCs at the elbow of a scree plot as input. Cluster identification was robust across a range of PCs and resolutions (Fig. S4A; see discussion of clustering robustness below).

Classification of type I and type II SGNs

To isolate subsets of SGNs, we performed iterative rounds of clustering and cell selection, which is a common procedure when analyzing single-cell data (Zheng et al., 2018). For the initial matrix of 17,556 cells, we identified 2,378 variable genes and 24 unique clusters using 60 PCs and a resolution of 0.3. To visualize the clusters, we computed the t-Distributed Stochastic Neighbor Embedding (tSNE) of the cells using the first 60 PCs and overlaid the cluster assignments on the first two dimensions (Fig. 1B and Fig. S2A). The resultant plot showed substantial separation of the majority of the clusters. In addition, a heatmap of the top 20 genes that were unique to each cluster based on average log fold-change showed a high degree of heterogeneity between the clusters (Fig. S2B). Based on expression of known marker genes, the non-neuronal clusters represented a diverse array of cell types, including hair cells, epithelial cells, immune cells, glia, mesenchymal cells, fibrocytes, and interdental cells (data not shown). As discussed in the main text, three clusters were putative type I SGNs and one cluster was putative type II SGNs (Fig. S2C and Fig. S3). Since SGNs are the focus of this report, further analysis of the non-neuronal clusters is not presented.

The initial clustering analysis revealed potential subtype heterogeneity amongst the putative type I SGNs (Fig. S4B). To eliminate unwanted sources of variation on the clustering process potentially driven by the influence of other cell types, we selected the four putative SGN groups and repeated the clustering analysis to isolate specific differences amongst these cells. We identified 1,634 variable genes and 10 clusters using 30 PCs and a resolution of 0.3 (Fig. S5). The smallest of the ten clusters segregated on the first PC of a PCA, had low UMI complexity, and showed low expression levels of canonical SGN genes like *Nefh*, *Nefl*, and *Tubb3* (cluster 9 in Fig. S5F), suggesting it was substantially different from the other SGNs. In addition, cells in this cluster expressed significantly higher levels of *Npy*, a gene which can be expressed in either neurons or glia (Ubink et al., 2003). Another cluster

did express canonical SGN genes but showed elevated levels of *Coch* (cluster 6 in Fig. S5F), a gene that has previously been localized to fibrocytes (Robertson et al., 2001). This cluster of cells also separated from the majority of cells on PC1. Lastly, a third cluster of cells had very low UMI complexity that was well below the median for all cells (Fig. S5E; cluster 7 in Fig. S5F) and did not appear to express many unique genes. Based on these findings, we eliminated these three clusters (Fig. S5B). Of the remaining seven clusters, one represented type II SGNs based on expression of type II SGN genes like *Prph*, and the remaining six were type I SGNs (Fig. S5F). This final dataset of SGNs consisted of 6,113 type I and 95 type II cells (Fig. 1C). The removed cells represented <8% of the putative SGNs selected from the full matrix; however, it should be noted that 40% of the putative type II SGNs in Fig. 1B were eliminated.

Clustering robustness

In order to evaluate the robustness of our initial clustering and identification of neuronal populations, we performed clustering on the full matrix of 17,556 cells 25 times, varying the parameters. We varied the number of principal components used from 40 to 80, and the resolution parameter from 0.2 to 0.4. After each round of clustering, we recorded the identities of type I and type II neurons, as well as the identities to which all other cells were assigned. Finally, we computed a consensus matrix, in which each value corresponds to the number of times each pair of cells was identified as the same cell type (Fig. S4A). Thus, for the identification of gross neuronal identity, the clustering analysis was insensitive to a range of PCs and resolutions.

Classification of type I SGN subtypes

Both clustering analyses suggested there was additional heterogeneity amongst type I SGNs. To explore this further, we selected all type I SGNs from the final dataset and performed a third round of clustering. Physiological recordings indicate at least three subtypes, so we systematically altered the resolution parameter until three clusters emerged (2,282 variable genes, 22 PCs, and a resolution parameter of 0.15). As subsequent histological validation confirmed (Fig. 2), these clusters represented true biological variation and not sample bias (Fig. S7A) or glial contamination (see more in-depth discussion of the effects of glia contamination below).

Increasing the resolution parameter to 0.2 led to the identification of 2 additional clusters; however, examination of marker genes (highest average log fold-change of significant genes from pairwise comparisons) revealed glia-specific genes like *Mpz*, *Pmp22*, *Mbp*, and *Mpzl1*. Thus, glial contamination appeared to be the next largest source of variation that drove clustering within the dataset. This was not surprising given that the most negative loadings on several of the PCs were glia-specific genes.

We wondered whether further biological heterogeneity existed within the dataset, and was masked by PCs representing glial contamination. In addition, since PCA only finds maximum sources of variance, each PC can potentially represent multiple cell types. Independent component analysis (ICA), on the other hand, seeks to identify basis vectors that are statistically independent, and it has been successfully employed to separate subtle

differences between cells in scRNA-Seq data (Trapnell et al., 2014; Zheng et al., 2018). Therefore, we applied Seurat's clustering procedure using ICA instead of PCA. The elbow in the scree plot occurred at the eighth IC, and the gene loadings revealed that IC1 and IC8 likely represented the previously identified Type IA, B, and C clusters. Except for IC2, the remaining ICs were either glial cells or redundant. Using these ICs (1, 2, and 8), we re-clustered the cells, and found that a resolution parameter of 0.1 recapitulated the original 3 clusters with >90% agreement (Fig. S7C). Furthermore, increasing the resolution to 0.3 split the original 3 clusters into 6 (Fig. S7D-E). Contaminating glial gene expression was evenly distributed, indicating that glial contamination did not drive clustering (Fig. 7E).

Differential expression analysis

All differential expression analysis was performed using MAST (Finak et al., 2015). Briefly, we fit a two-part generalized linear model, which allowed us to model both the rate of expression of a gene over background, as well as the positive expression mean. Prior to differential expression testing, the gene expression matrix was filtered to only include genes expressed in > 5% of all cells. The sample of origin and the variable of interest (e.g. subtype) were modeled as a mixed and fixed effect, respectively. The gene complexity of each cell was also included as a fixed effect. A likelihood ratio test was used to determine the significance values, and p-values were adjusted for multiple hypothesis testing using the Benjamini-Hochberg method. Genes with an adjusted p-value < 0.01 and an absolute log-fold change > 0.1 were counted as significant. Significant hits from all differential expression analyses are reported in Tables S2-S9. Table S10 lists the genes that comprise the six functional categories of molecules as described by Paul et al. (Paul et al., 2017). The differentially expressed genes in Tables S3-S5 were cross-referenced with this list to identify the genes shown in Figure 3A.

Effects of glial contamination

In mice, both the peripheral fibers and soma of most type I SGNs are myelinated, and the soma are also surrounded by satellite glial cells. Given the strong adhesions between these cell types, it is difficult to fully dissociate SGNs from glia. Thus, we expected that many of the droplets consisted of co-captures of neurons and glia. Indeed, the SGN clusters identified in Fig. 1B and Fig. S2A had detectable levels of glia-specific transcripts like *Mpz*, *Pmp22*, *Mbp*, and *Mpzl1*, albeit the levels were significantly lower than in the cluster of pure glial cells (Fig. S6A-B). Some cells showed less contamination than others, which contributed to the clustering presented in Fig. S5A (Fig. S6C-D).

As described above, glial contamination did not appear to contribute to the clustering type I SGNs into three major subtypes. However, to be certain of this, we selected the type I SGNs that had lower levels of glial gene contamination (i.e. clusters 4 and 5 in Fig. S6C), and repeated the clustering procedure to extract three clusters from the dataset. The three clusters appeared to be grossly identical to those identified in the full dataset, and the genes that were differentially expressed between subtypes in the full and non-contaminated datasets were highly correlated (Fig. S6E-G; Tables S7-S9). Lastly, there was little overlap in genes that were differentially expressed between subtypes in the non-contaminated dataset compared to genes that were differentially expressed between contaminated and non-contaminated type I

SGNs (Fig. S6H; Tables S6-S9). The glia specific genes identified in the latter analysis (Table S6) had 87% overlap with genes that were differentially expressed between all type I SGNs and pure glia (clusters 0, 1, and 4 versus cluster 2 in Fig. S2A).

Immunofluorescence

For immunofluorescent studies, cochlea was dissected from mice perfused with 20 ml 0.1 M PBS (pH 7.4) followed with 25 ml of fixative (4% formaldehyde (vol/vol)). After post-fixation overnight in 4 °C, tissues were decalcified in 100mM EDTA for 2–3 days, cryoprotected in 30% sucrose (wt/vol) for 12 h and then sectioned with a cryostat at 16 μm. The sections on slides were dried at 37 °C for 40 min, and fixed with 4% paraformaldehyde at room temperature for 10 min. The slides were pre-incubated in blocking solution (10% normal goat serum (vol/vol), 0.2% Triton X-100 (vol/vol) in PBS, pH 7.4) for 1h at room temperature, then incubated overnight at 4 °C with primary antibodies. Secondary antibody incubation was performed at room temperature for 2 h. After rinsing in PBS, samples were cover-slipped with Vectashield. Labeled sections were imaged using a Zeiss 700 Confocal Laser Microscope System.

For primary antibodies, we used goat α-CALB2 (CG1, Swant, 1:2500), mouse α-CALB2 (MAB1568, Millipore, 1:1000), mouse α-TuJ1 (801201, Biolegend, 1:400), rabbit α-TuJ1 (SAB4500088, Sigma, 1:200), mouse α-POU4F1 (MAB1585, Millipore, 1:20), rabbit α-CALB1 (13176, New England Biolabs, 1:50), rabbit α-Tyrosine Hydroxylase (657012, Millipore, 1:1000) and rabbit α-p75 NGFR (Weskamp et al., 1991, 1:800). For secondary antibodies, we used goat α-rabbit (A11008, Alexa 488 conjugated; A11011, Alexa 568 conjugated, Thermo Fisher), goat α-mouse (A11001. Alexa 488 conjugated; A11004, Alexa 568 conjugated, Thermo Fisher), donkey α-goat (A11055, Alexa 488 conjugated) and donkey α-mouse (A10037, Alexa 568 conjugated). All secondary antibodies were diluted 1:500 in blocking solution.

Serial sections were analyzed from at least three animals for each genotype and the number of neurons expressing molecular markers was determined in each section. Data analysis was performed using Excel (Microsoft, Redmond, WA) and R (MathWorks, Natick, MA). All data are presented as mean ± SEM. Student's two-tailed paired or unpaired t-test was used to determine statistical significance between measurements in the same cohort or different cohorts, respectively (*$p < 0.05$, **$p < 0.01$, ***$p < 0.001$). Data are also presented in the main text and in the figure legends.

RNAscope *in situ* hybridization

Fixed frozen sections were obtained as described above at 14 μm. RNAscope Multiplex Fluorescent Reagent Kit and RNAscope 2.5 HD reagent kit-RED (Advanced Cell Diagnostics) were used according to the user manual for fixed frozen tissues. Target probes for *Lypd1*, *Calb2* and *Pou4f1* were used in experiments. Data collection, quantification and statistical analysis was carried out as describe in the previous section (Immunofluorescence). Data are also presented in the main text and in the figure legends.

Electrophysiology

Cochleae were dissected from postnatal day 5–7 control (*Tmie*$^{+/+ \text{ or } +/-}$; *Vglut3*$^{+/+ \text{ or } +/-}$), *Tmie-ko,* and *Vglut3-ko* mice, as described previously (Tritsch et al., 2007; Zhang-Hooks et al., 2016), in ice-cold, sterile-filtered HEPES-buffered artificial cerebrospinal fluid (aCSF) consisting of the following (in mM): 130 NaCl, 2.5 KCl, 10 HEPES, 1 NaH_2PO_4, 1.3 $MgCl_2$, 2.5 $CaCl_2$, and 11 D-Glucose. Explants were mounted onto Cell-Tak (Corning) treated coverslips and incubated at 37º C for 24 hours in Dulbecco's modified Eagle's medium (F-12/DMEM; Invitrogen) supplemented with 1% fetal bovine serum (FBS) and 10U/mL penicillin (Sigma) prior to recording.

For juxtacellular recordings, cochleae were transferred to a recording chamber and continuously superfused with bicarbonate-buffered aCSF at 1.5 – 2 mL/min, consisting of the following (in mM): 115 NaCl, 6 KCl, 1.3 $MgCl_2$, 1.3 $CaCl_2$, 1 NaH_2PO_4, 26.2 $NaHCO_3$, 11 D-glucose, and saturated with 95% O_2 / 5% CO_2 to maintain a pH of 7.4. Recordings were performed at near physiological temperature (32–34ºC) using a feedback-controlled in-line heater (Warner Instruments). Electrodes for SGN recordings had tip resistances between 1.5–2.5 MΩ when filled with artificial cerebrospinal fluid. Extracellular potentials were recorded for 10 minutes with pClamp10 software using a Multiclamp 700B amplifier, low pass filtered at 20 kHz, and digitized at 50 kHz with a Digidata 1322A analog-to-digital converter (Axon Instruments). SGNs that displayed tonic firing indicative of cellular pathology were not included in the analysis datasets. For d-tubocurarine (d-TC) experiments, spikes were analyzed in five-minute windows; five minutes of baseline preceded ten minutes of superfusion of aCSF containing 50 μM d-TC and a ten-minute wash period. Firing behavior in the latter five minutes of baseline, drug and wash were analyzed.

Data were analyzed offline using custom routines written in Matlab 2017b (Mathworks). Briefly, raw traces were high-pass filtered to remove baseline drift and spikes were identified using an amplitude threshold criterion. As described previously (Tritsch et al., 2010), bursts were identified by classifying interspike intervals into non-bursting intervals (> 1 s), burst intervals (30 ms - 1 s), and mini-burst intervals (< 30 ms). Bursts were defined as clusters of at least 10 consecutive burst intervals (with mini-burst intervals being ignored in the context of burst detection). Spikes within mini-bursts were included when calculating the number of spikes within a burst. Colored raster plots were generated by grouping spikes into one-second bins and applying a color map to the resulting data (modified 'hot' colormap; Matlab). All values are mean ± SEM. Statistical significance was calculated with two-tailed paired t-test, Bonferroni correction applied; ** $p<0.01$, * $p<0.05$, ns: not significant. Data are also presented in the main text and in the figure legends. The exact number of cells analyzed is indicated in Fig. 7.

Supplementary Material

Refer to Web version on PubMed Central for supplementary material.

ACKNOWLEDGEMENT

This research was funded by NIDCD grants DC005965, DC007704, DC014713 (UM); DC008060 (DB); and a grant from the Rubenstein Fund for Hearing Research (DB and UM).

REFERENCES

Alagramam KN, Goodyear RJ, Geng R, Furness DN, van Aken AF, Marcotti W, Kros CJ, and Richardson GP (2011). Mutations in protocadherin 15 and cadherin 23 affect tip links and mechanotransduction in mammalian sensory hair cells. PLoS One 6, e19183. [PubMed: 21532990]

Arroyo DA, and Feller MB (2016). Spatiotemporal Features of Retinal Waves Instruct the Wiring of the Visual Circuitry. Front Neural Circuits 10, 54. [PubMed: 27507937]

Barclay M, Ryan AF, and Housley GD (2011). Type I vs type II spiral ganglion neurons exhibit differential survival and neuritogenesis during cochlear development. Neural Dev 6, 33. [PubMed: 21989106]

Beutner D, and Moser T (2001). The presynaptic function of mouse cochlear inner hair cells during development of hearing. J Neurosci 21, 4593–4599. [PubMed: 11425887]

Borgius L, Restrepo CE, Leao RN, Saleh N, and Kiehn O (2010). A transgenic mouse line for molecular genetic analysis of excitatory glutamatergic neurons. Mol Cell Neurosci 45, 245–257. [PubMed: 20600924]

Butler A, Hoffman P, Smibert P, Papalexi E, and Satija R (2018). Integrating single-cell transcriptomic data across different conditions, technologies, and species. Nat Biotechnol.

Calvo SE, Clauser KR, and Mootha VK (2016). MitoCarta2.0: an updated inventory of mammalian mitochondrial proteins. Nucleic Acid Res 44, 1251–1257.

Cohen-Cory S (2002). The developing synapse: construction and modulation of synaptic structures and circuits. Science 298, 770–776. [PubMed: 12399577]

D'Alessandro A, Righetti PG, and Zolla L (2010). The red blood cell proteome and interactome: an update. J Proteome Res 9, 144–163. [PubMed: 19886704]

Davis RL, and Crozier RA (2015). Dynamic firing properties of type I spiral ganglion neurons. Cell Tissue Res 361, 115–127. [PubMed: 25567109]

Dobin A, Davis CA, Schlesinger F, Drenkow J, Zaleski C, Jha S, Batut P, Chaisson M, and Gingeras TR (2013). STAR: ultrafast universal RNA-seq aligner. Bioinformatics 29, 15–21. [PubMed: 23104886]

Dror AA, and Avraham KB (2010). Hearing impairment: a panoply of genes and functions. Neuron 68, 293–308. [PubMed: 20955936]

Echteler SM (1992). Developmental segregation in the afferent projections to mammalian auditory hair cells. Proc Natl Acad Sci U S A 89, 6324–6327. [PubMed: 1631126]

Ehret G (1983). Development of hearing and response to behavior to sound stimuli: behavioral studies In: Roand R (ed) Development of t auditory and vestibular systems Academic, New York, 211–237.

Elder GA, Friedrich VL, Jr., Kang C, Bosco P, Gourov A, Tu PH, Zhang B, Lee VM, and Lazzarini RA (1998). Requirement of heavy neurofilament subunit in the development of axons with large calibers. J Cell Biol 143, 195–205. [PubMed: 9763431]

Finak G, McDavid A, Yajima M, Deng J, Gersuk V, Shalek AK, Slichter CK, Miller HW, McElrath MJ, Prlic M, et al. (2015). MAST: a flexible statistical framework for assessing transcriptional changes and characterizing heterogeneity in single-cell RNA sequencing data. Genome Biol 16, 278. [PubMed: 26653891]

Flores EN, Duggan A, Madathany T, Hogan AK, Marquez FG, Kumar G, Seal RP, Edwards RH, Liberman MC, and Garcia-Anoveros J (2015). A non-canonical pathway from cochlea to brain signals tissue-damaging noise. Curr Biol 25, 606–612. [PubMed: 25639244]

Fritzsch B, Silos-Santiago I, Bianchi LM, and Farinas I (1997). The role of neurotrophic factors in regulating the development of inner ear innervation. Trends Neurosci 20, 159–164. [PubMed: 9106356]

Furman AC, Kujawa SG, and Liberman MC (2013). Noise-induced cochlear neuropathy is selective for fibers with low spontaneous rates. J Neurophysiol 110, 577–586. [PubMed: 23596328]

Gillespie PG, and Muller U (2009). Mechanotransduction by hair cells: models, molecules, and mechanisms. Cell 139, 33–44. [PubMed: 19804752]

Glowatzki E, and Fuchs PA (2002). Transmitter release at the hair cell ribbon synapse. Nat Neurosci 5, 147–154. [PubMed: 11802170]

Hafidi A (1998). Peripherin-like immunoreactivity in type II spiral ganglion cell body and projections. Brain Res 805, 181–190. [PubMed: 9733963]

Heffner HE, Heffner RS, Contos C, and Ott T (1994). Audiogram of the hooded Norway rat. Hear Res 73, 244–247. [PubMed: 8188553]

Heil P, and Peterson AJ (2015). Basic response properties of auditory nerve fibers: a review. Cell Tissue Res 361, 129–158. [PubMed: 25920587]

Hoffman PN, Cleveland DW, Griffin JW, Landes PW, Cowan NJ, and Price DL (1987). Neurofilament gene expression: a major determinant of axonal caliber. Proc Natl Acad Sci U S A 84, 3472–3476. [PubMed: 3472217]

Huang EJ, and Reichardt LF (2003). Trk receptors: roles in neuronal signal transduction. Annu Rev Biochem 72, 609–642. [PubMed: 12676795]

Huang LC, Barclay M, Lee K, Peter S, Housley GD, Thorne PR, and Montgomery JM (2012). Synaptic profiles during neurite extension, refinement and retraction in the developing cochlea. Neural Dev 7, 38. [PubMed: 23217150]

Huang LC, Thorne PR, Housley GD, and Montgomery JM (2007). Spatiotemporal definition of neurite outgrowth, refinement and retraction in the developing mouse cochlea. Development 134, 2925–2933. [PubMed: 17626062]

Huberman AD, Feller MB, and Chapman B (2008). Mechanisms underlying development of visual maps and receptive fields. Annu Rev Neurosci 31, 479–509. [PubMed: 18558864]

Johnson SL, Marcotti W, and Kros CJ (2005). Increase in efficiency and reduction in Ca2+ dependence of exocytosis during development of mouse inner hair cells. J Physiol 563, 177–191. [PubMed: 15613377]

Kandler K (2004). Activity-dependent organization of inhibitory circuits: lessons from the auditory system. Curr Opin Neurobiol 14, 96–104. [PubMed: 15018944]

Kandler K, Clause A, and Noh J (2009). Tonotopic reorganization of developing auditory brainstem circuits. Nat Neurosci 12, 711–717. [PubMed: 19471270]

Kandler K, and Gillespie DC (2005). Developmental refinement of inhibitory sound-localization circuits. Trends Neurosci 28, 290–296. [PubMed: 15927684]

Kim KX, and Fettiplace R (2013). Developmental changes in the cochlear hair cell mechanotransducer channel and their regulation by transmembrane channel-like proteins. J Gen Physiol 141, 141–148. [PubMed: 23277480]

Koay G, Heffner R, and Heffner H (2002). Behavioral audiograms of homozygous med(J) mutant mice with sodium channel deficiency and unaffected controls. Hear Res 171, 111–118. [PubMed: 12204355]

Koundakjian EJ, Appler JL, and Goodrich LV (2007). Auditory neurons make stereotyped wiring decisions before maturation of their targets. J Neurosci 27, 14078–14088. [PubMed: 18094247]

Lallemend F, Vandenbosch R, Hadjab S, Bodson M, Breuskin I, Moonen G, Lefebvre PP, and Malgrange B (2007). New insights into peripherin expression in cochlear neurons. Neuroscience 150, 212–222. [PubMed: 17964735]

Lelli A, Asai Y, Forge A, Holt JR, and Geleoc GS (2009). Tonotopic gradient in the developmental acquisition of sensory transduction in outer hair cells of the mouse cochlea. J Neurophysiol 101, 2961–2973. [PubMed: 19339464]

Liberman LD, and Liberman MC (2016). Postnatal maturation of auditory-nerve heterogeneity, as seen in spatial gradients of synapse morphology in the inner hair cell area. Hear Res 339, 12–22. [PubMed: 27288592]

Liberman LD, Wang H, and Liberman MC (2011). Opposing gradients of ribbon size and AMPA receptor expression underlie sensitivity differences among cochlear-nerve/hair-cell synapses. J Neurosci 31, 801–808. [PubMed: 21248103]

Liberman MC (1978a). Auditory-nerve response from cats raised in a low-noise chamber. J Acoust Soc Am 63, 442–455. [PubMed: 670542]

Liberman MC (1978b). Auditory-nerve responses from cats raised in low-noise chamber. J Acoust Soc Am 63, 442–453. [PubMed: 670542]

Liberman MC (1980). Morphological differences among radial afferent fibers in the cat cochlea: an electron-microscopic study of serial sections. Hear Res 3, 45–63. [PubMed: 7400048]

Liberman MC (1982). Single-neuron labeling in the cat auditory nerve. Science 216, 1239–1241. [PubMed: 7079757]

Liberman MC (2017). Noise-induced and age-related hearing loss: new perspectives and potential therapies. F1000Res 6, 927. [PubMed: 28690836]

Liu C, Glowatzki E, and Fuchs PA (2015). Unmyelinated type II afferent neurons report cochlear damage. Proc Natl Acad Sci U S A 112, 14723–14727. [PubMed: 26553995]

Liu Q, and Davis RL (2007). Regional specification of threshold sensitivity and response time in CBA/CaJ mouse spiral ganglion neurons. J Neurophysiol 98, 2215–2222. [PubMed: 17715200]

Liu Q, Lee E, and Davis RL (2014). Heterogeneous intrinsic excitability of murine spiral ganglion neurons is determined by Kv1 and HCN channels. Neuroscience 257, 96–110. [PubMed: 24200924]

Lu B, Pang PT, and Woo NH (2005). The yin and yang of neurotrophin action. Nat Rev Neurosci 6, 603–614. [PubMed: 16062169]

Macosko EZ, Basu A, Satija R, Nemesh J, Shekhar K, Goldman M, Tirosh I, Bialas AR, Kamitaki N, Martersteck EM, et al. (2015). Highly Parallel Genome-wide Expression Profiling of Individual Cells Using Nanoliter Droplets. Cell 161, 1202–1214. [PubMed: 26000488]

Madisen L, Zwingman TA, Sunkin SM, Oh SW, Zariwala HA, Gu H, Ng LL, Palmiter RD, Hawrylycz MJ, Jones AR, et al. (2010). A robust and high-throughput Cre reporting and characterization system for the whole mouse brain. Nat Neurosci 13, 133–140. [PubMed: 20023653]

Marszalek JR, Williamson TL, Lee MK, Xu Z, Hoffman PN, Becher MW, Crawford TO, and Cleveland DW (1996). Neurofilament subunit NF-H modulates axonal diameter by selectively slowing neurofilament transport. J Cell Biol 135, 711–724. [PubMed: 8909545]

Merchan-Perez A, and Liberman MC (1996). Ultrastructural differences among afferent synapses on cochlear hair cells: correlations with spontaneous discharge rate. J Comp Neurol 371, 208–221. [PubMed: 8835727]

Meyer AC, and Moser T (2010). Structure and function of cochlear afferent innervation. Curr Opin Otolaryngol Head Neck Surg 18, 441–446. [PubMed: 20802334]

Mikaelian D, and Ruben RJ (1965). Development of hearing in the normal Cba-J mouse: correlation of physiological observations with behavioral responses and with cochlear anatomy. Acta Otolaryngol 59, 451–461.

Mou K, Adamson CL, and Davis RL (1998). Time-dependence and cell-type specificity of synergistic neurotrophin actions on spiral ganglion neurons. J Comp Neurol 402, 129–139. [PubMed: 9831050]

Nishimura K, Noda T, and Dabdoub A (2017). Dynamic Expression of Sox2, Gata3, and Prox1 during Primary Auditory Neuron Development in the Mammalian Cochlea. PLoS One 12, e0170568. [PubMed: 28118374]

Pan B, Geleoc GS, Asai Y, Horwitz GC, Kurima K, Ishikawa K, Kawashima Y, Griffith AJ, and Holt JR (2013). TMC1 and TMC2 are components of the mechanotransduction channel in hair cells of the mammalian inner ear. Neuron 79, 504–515. [PubMed: 23871232]

Paul A, Crow M, Raudales R, He M, Gillis J, and Huang ZJ (2017). Transcriptional Architecture of Synaptic Communication Delineates GABAergic Neuron Identity. Cell 171, 522–539 e520. [PubMed: 28942923]

Perkins RE, and Morest DK (1975). A study of cochlear innervation patterns in cats and rats with the Golgi method and Nomarkski Optics. J Comp Neurol 163, 129–158. [PubMed: 1100684]

Richardson GP, de Monvel JB, and Petit C (2011). How the genetics of deafness illuminates auditory physiology. Annu Rev Physiol 73, 311–334. [PubMed: 21073336]

Robertson D, and Paki B (2002). Role of L-type Ca2+ channels in transmitter release from mammalian inner hair cells. II. Single-neuron activity. J Neurophysiol 87, 2734–2740. [PubMed: 12037175]

Robertson NG, Resendes BL, Lin JS, Lee C, Aster JC, Adams JC, and Morton CC (2001). Inner ear localization of mRNA and protein products of COCH, mutated in the sensorineural deafness and vestibular disorder, DFNA9. Hum Mol Genet 10, 2493–2500. [PubMed: 11709536]

Ruel J, Emery S, Nouvian R, Bersot T, Amilhon B, Van Rybroek JM, Rebillard G, Lenoir M, Eybalin M, Delprat B, et al. (2008). Impairment of SLC17A8 encoding vesicular glutamate transporter-3, VGLUT3, underlies nonsyndromic deafness DFNA25 and inner hair cell dysfunction in null mice. Am J Hum Genet 83, 278–292. [PubMed: 18674745]

Ruggero MA, and Temchin AN (2002). The roles of the external, middle, and inner ears in determining the bandwidth of hearing. Proc Natl Acad Sci U S A 99, 13206–13210. [PubMed: 12239353]

Ryugo DK (1992). The auditory nerve: peripheral innervatio cell body morphology, and central projections . In: The mammalian auditory pathway: neuroanatomy (Popper AN, Fay RR eds), 34–93. New York: Springer.

Satija R, Farrell JA, Gennert D, Schier AF, and Regev A (2015). Spatial reconstruction of single-cell gene expression data. Nat Biotechnol 33, 495–502. [PubMed: 25867923]

Schmiedt RA, Mills JH, and Boettcher FA (1996). Age-related loss of activity of auditory-nerve fibers. J Neurophysiol 76, 2799–2803. [PubMed: 8899648]

Seal RP, Akil O, Yi E, Weber CM, Grant L, Yoo J, Clause A, Kandler K, Noebels JL, Glowatzki E, et al. (2008). Sensorineural deafness and seizures in mice lacking vesicular glutamate transporter 3. Neuron 57, 263–275. [PubMed: 18215623]

Simmons DD (1994). A transient afferent innervation of outer hair cells in the postnatal cochlea. Neuroreport 5, 1309–1312. [PubMed: 7919186]

Sobkowicz HM, Rose JE, Scott GL, and Levenick CV (1986). Distribution of synaptic ribbons in the developing organ of Corti. J Neurocytol 15, 693–714. [PubMed: 3819777]

Sonntag M, Englitz B, Kopp-Scheinpflug C, and Rubsamen R (2009). Early postnatal development of spontaneous and acoustically evoked discharge activity of principal cells of the medial nucleus of the trapezoid body: an in vivo study in mice. J Neurosci 29, 9510–9520. [PubMed: 19641114]

Spoendlin H (1973). The innervation of the cochlea receptor In: Mechanisms in hearing (Moller AR, ed), pp185–229. New York: Academic.

Taberner AM, and Liberman MC (2005). Response properties of single auditory nerve fibers in the mouse. J Neurophysiol 93, 557–569. [PubMed: 15456804]

Trapnell C, Cacchiarelli D, Grimsby J, Pokharel P, Li S, Morse M, Lennon NJ, Livak KJ, Mikkelsen TS, and Rinn JL (2014). The dynamics and regulators of cell fate decisions are revealed by pseudotemporal ordering of single cells. Nat Biotechnol 32, 381–386. [PubMed: 24658644]

Tritsch NX, and Bergles DE (2010). Developmental regulation of spontaneous activity in the Mammalian cochlea. J Neurosci 30, 1539–1550. [PubMed: 20107081]

Tritsch NX, Rodriguez-Contreras A, Crins TT, Wang HC, Borst JG, and Bergles DE (2010). Calcium action potentials in hair cells pattern auditory neuron activity before hearing onset. Nat Neurosci 13, 1050–1052. [PubMed: 20676105]

Tritsch NX, Yi E, Gale JE, Glowatzki E, and Bergles DE (2007). The origin of spontaneous activity in the developing auditory system. Nature 450, 50–55. [PubMed: 17972875]

Ubink R, Calza L, and Hokfelt T (2003). 'Neuro'-peptides in glia: focus on NPY and galanin. Trends Neurosci 26, 604–609. [PubMed: 14585600]

Vyas P, Wu JS, Zimmerman A, Fuchs P, and Glowatzki E (2017). Tyrosine Hydroxylase Expression in Type II Cochlear Afferents in Mice. J Assoc Res Otolaryngol 18, 139–151. [PubMed: 27696081]

Wang HC, and Bergles DE (2015). Spontaneous activity in the developing auditory system. Cell Tissue Res 361, 65–75. [PubMed: 25296716]

Wang HC, Lin CC, Cheung R, Zhang-Hooks Y, Agarwal A, Ellis-Davies G, Rock J, and Bergles DE (2015). Spontaneous Activity of Cochlear Hair Cells Triggered by Fluid Secretion Mechanism in Adjacent Support Cells. Cell 163, 1348–1359. [PubMed: 26627734]

Wu JS, Young ED, and Glowatzki E (2016). Maturation of Spontaneous Firing Properties after Hearing Onset in Rat Auditory Nerve Fibers: Spontaneous Rates, Refractoriness, and Interfiber Correlations. J Neurosci 36, 10584–10597. [PubMed: 27733610]

Xiang M, Gan L, Li D, Chen ZY, Zhou L, O'Malley BW, Jr., Klein W, and Nathans J (1997). Essential role of POU-domain factor Brn-3c in auditory and vestibular hair cell development. Proc Natl Acad Sci U S A 94, 9445–9450. [PubMed: 9256502]

Xiong W, Grillet N, Elledge HM, Wagner TF, Zhao B, Johnson KR, Kazmierczak P, and Muller U (2012). TMHS is an integral component of the mechanotransduction machinery of cochlear hair cells. Cell 151, 1283–1295. [PubMed: 23217710]

Xu Z, Marszalek JR, Lee MK, Wong PC, Folmer J, Crawford TO, Hsieh ST, Griffin JW, and Cleveland DW (1996). Subunit composition of neurofilaments specifies axonal diameter. J Cell Biol 133, 1061–1069. [PubMed: 8655579]

Zeisel A, Munoz-Manchado AB, Codeluppi S, Lonnerberg P, La Manno G, Jureus A, Marques S, Munguba H, He L, Betsholtz C, et al. (2015). Brain structure. Cell types in the mouse cortex and hippocampus revealed by single-cell RNA-seq. Science 347, 1138–1142. [PubMed: 25700174]

Zhang-Hooks Y, Agarwal A, Mishina M, and Bergles DE (2016). NMDA Receptors Enhance Spontaneous Activity and Promote Neuronal Survival in the Developing Cochlea. Neuron 89, 337–350. [PubMed: 26774161]

Zhao B, and Muller U (2015). The elusive mechanotransduction machinery of hair cells. Curr Opin Neurobiol 34, 172–179. [PubMed: 26342686]

Zhao B, Wu Z, Grillet N, Yan L, Xiong W, Harkins-Perry S, and Muller U (2014). TMIE is an essential component of the mechanotransduction machinery of cochlear hair cells. Neuron 84, 954–967. [PubMed: 25467981]

Zheng GX, Terry JM, Belgrader P, Ryvkin P, Bent ZW, Wilson R, Ziraldo SB, Wheeler TD, McDermott GP, Zhu J, et al. (2017). Massively parallel digital transcriptional profiling of single cells. Nat Commun 8, 14049. [PubMed: 28091601]

Zheng S, Papalexi E, Butler A, Stephenson W, and Satija R (2018). Molecular transitions in early progenitors during human cord blood hematopoiesis. Mol Syst Biol 14, e8041. [PubMed: 29545397]

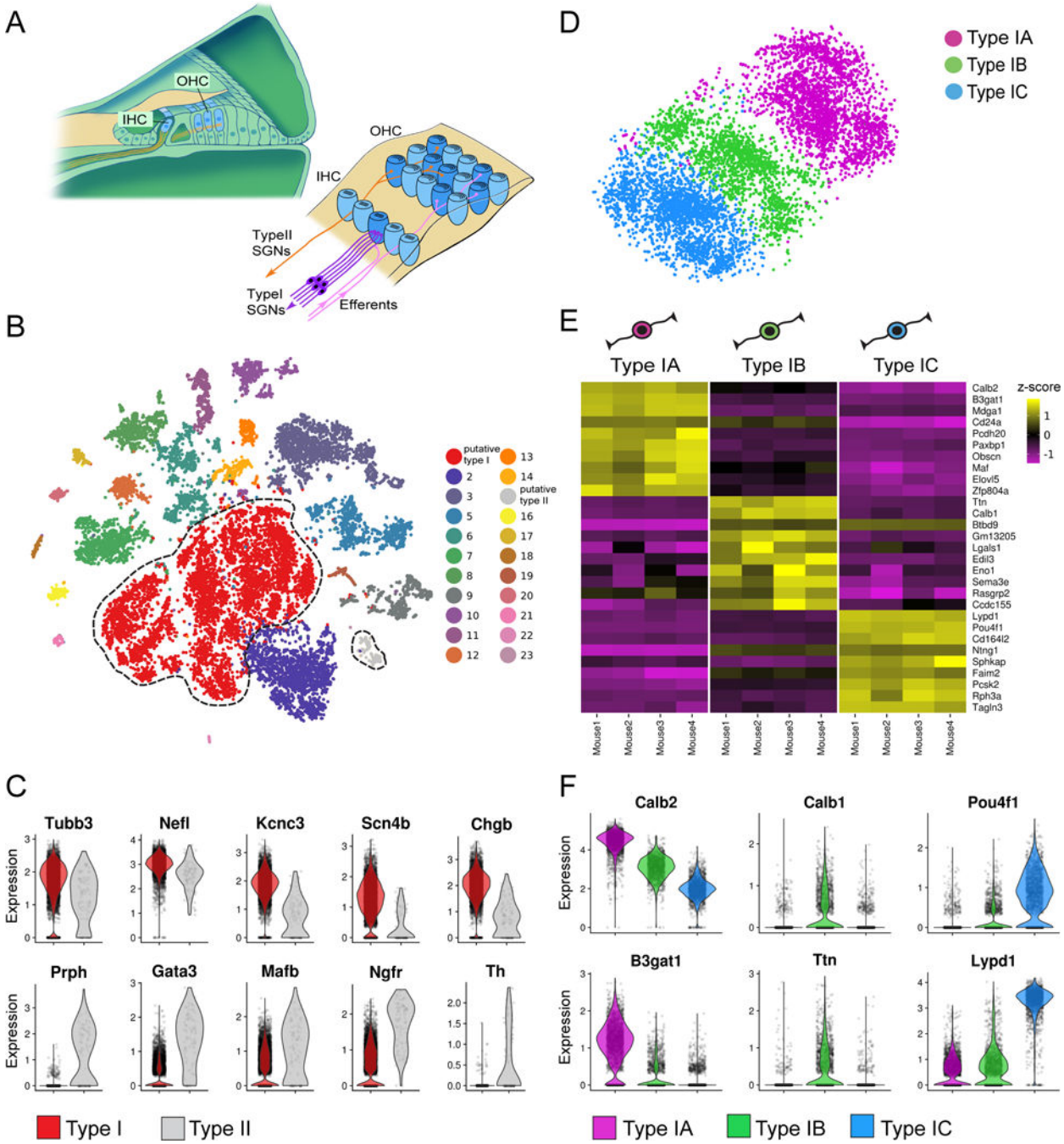

Fig. 1. Identification of subtype of type I SGNs by scRNA-seq.

(A) Diagram on the left: cochlear cross-section; inner hair cells, IHCs; outer hair cells, OHCs. Right: top view onto the sensory epithelium showing IHCs, OHCs and SGNs. Efferent neurons are shown in pink but are not studied here. (B) tSNE plot from the sensory compartment of the mouse inner ear at 9 weeks of age. Putative Type I SGNs (*Tubb3*$^{+}$) in red; putative type II SGNs (*Prph*$^{+}$) in grey. (C) Violin plots showing select genes that are differentially expressed between final sets of type I and type II SGNs (see Fig. S5A-B and Methods for SGNs refinement); y-axis is a log scale. (D) tSNE plot of type I SGNs showing

three subtypes (IA, IB, IC). (E) Heat maps showing standardized expression of the top 10 differentially expressed genes ($p<0.01$ from pairwise comparisons, highest average log-fold change). Expression is averaged across all cells from an individual mouse for each cluster. Rows are genes, columns are averages for each mouse, grouped by cluster. (F) Violin plots of select genes from (E) within subtypes. Y-axis in C and F, log-normalized transcript counts. See also Figure S1-S7, Table S1-S9, and the STAR Methods.

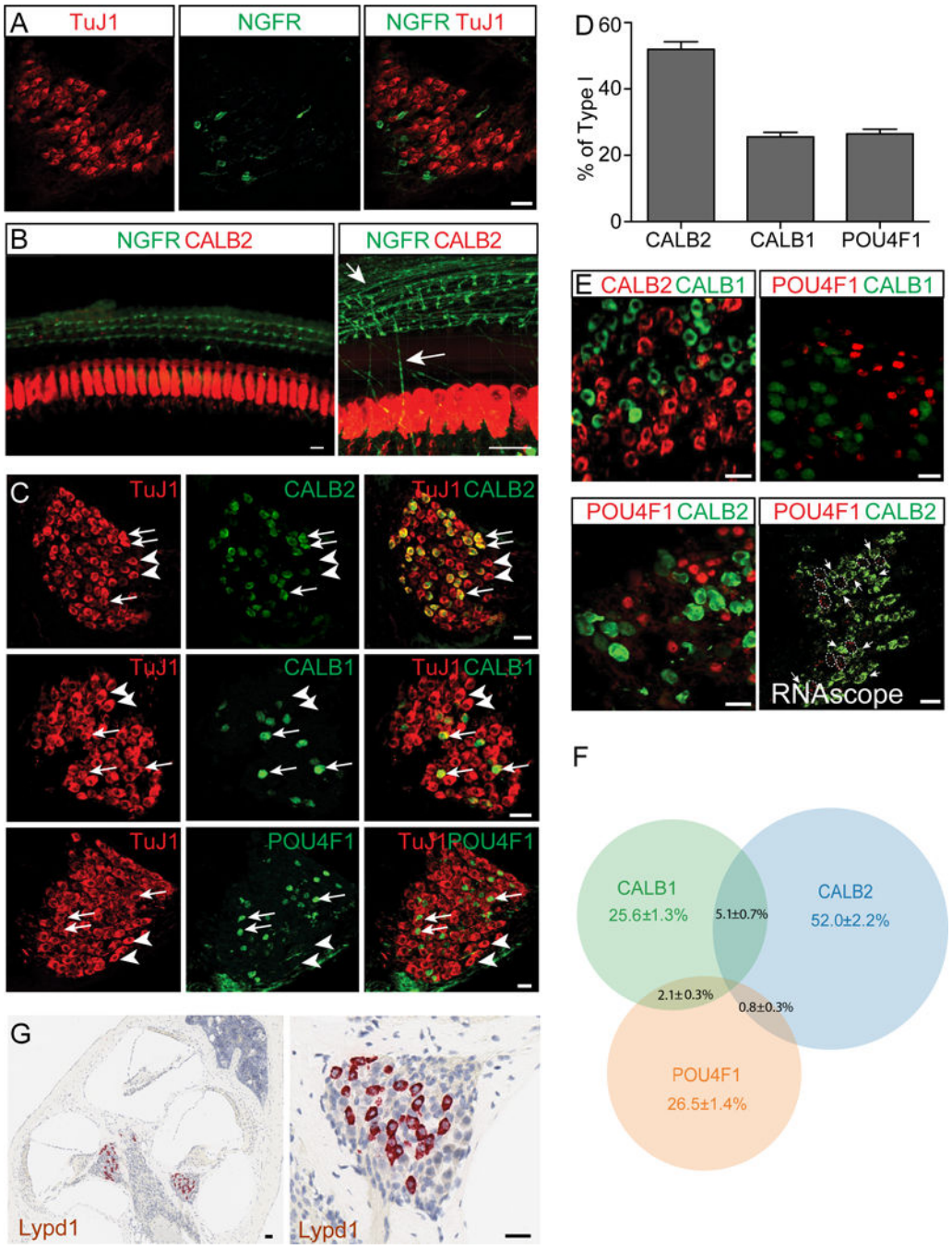

Fig. 2. Validation of molecular subtypes of SGNs.

(A) P28 sections stained with antibodies to TuJ1 (red) and NGFR (green) to identify type I and type II SGNs. (B) P28 cochlear whole mounts stained for CALB2 to label IHCs and for NGFR (green). Note labeling of type II nerve fibers (arrows) within the OHC region. (C) P28 sections stained with the indicated antibodies to distinguish type IA, IB, and IC SGNs (arrowheads: cells only expressing TuJ1; arrows: cells co-expressing TuJ1 with CALB2, CALB1 or POU4F1). (D) Percentage of type I SGNs expressing CALB2, CALB1 and POU4F1 at P28 (serial sections from three mice; values are mean ± SEM). (E) P28 sections

stained for CALB2, CALB1 and POU4F1. In bottom right panel, segregation of markers as determined by RNAscope. (F) Quantification of the percentage of type I SGNs co-expressing markers (serial sections from three mice; values are mean ± SEM). (G) RNAscope analysis of Lypd1 expression. Left: overview of the cochlea; right: spiral ganglion. Scale bars: 20μm.

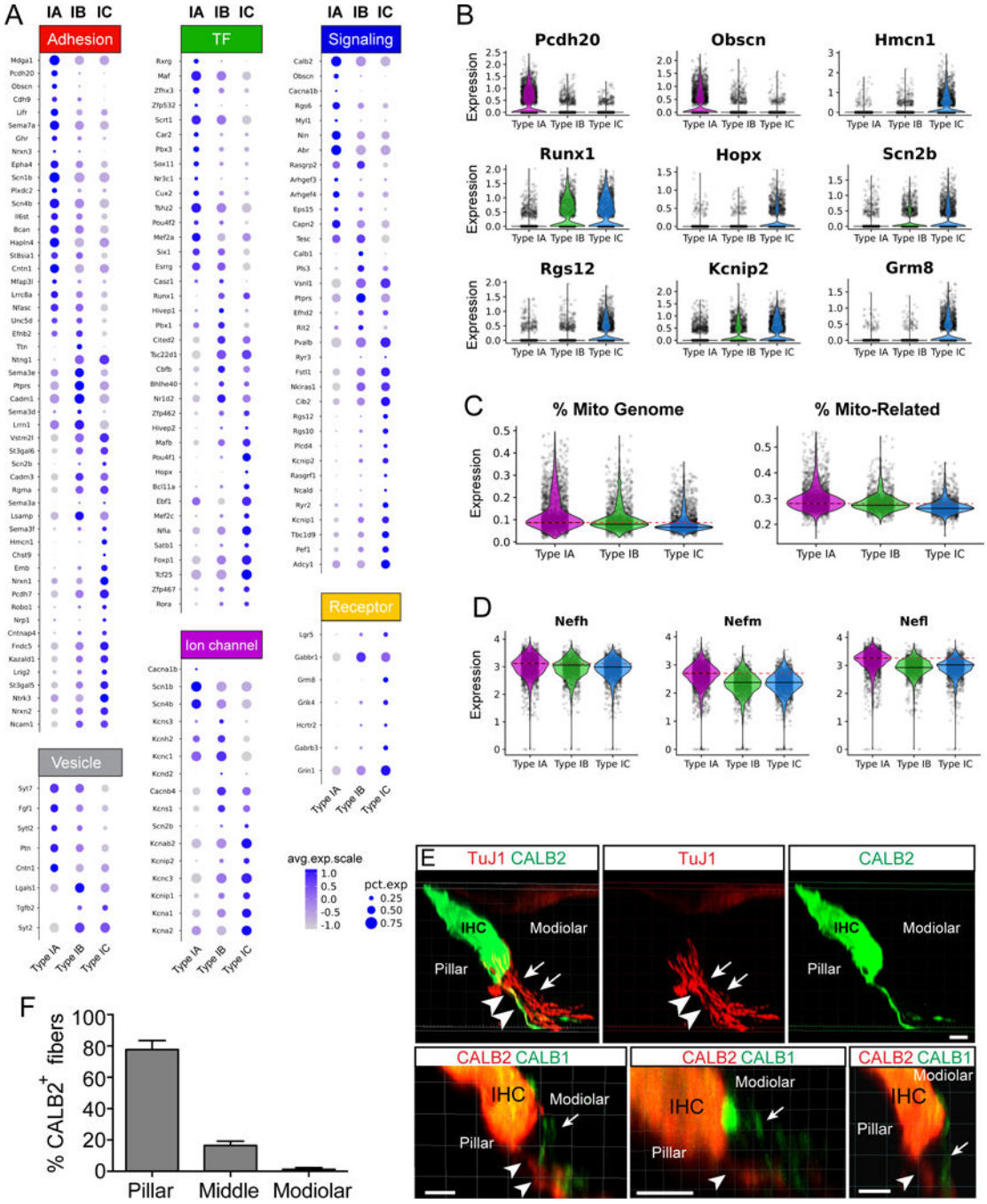

Fig. 3. Molecular characterization of type I SGN subtypes and innervation patterns.

(A) Dot plots showing differentially expressed genes (log fold-change >0.1 and p<0.01 from pairwise comparisons) in type I SGN subtypes grouped by functional category; color scale: average expression of all single cells in each cluster; dot size: percentage of single cells with detectable expression (>1 transcript). (B) Violin plots of select genes. (C) Violin plots of fraction of total transcripts in single cells from the 13 protein-coding genes in the mitochondrial genome and 1,092 cellular genes associated with mitochondrial function (Calvo et al., 2016). All pairwise comparisons are statistically significant (p<0.0001, nested

model ANOVA). (D) Violin plots of neurofilament gene expression. Lines in C and D indicate the peak density of cells in the violin plots. The dotted line is an extension of the line from type IA neurons to facilitate comparison. Y-axis in B and D, log-normalized transcript counts. Y-axis in C, fraction of total transcripts in each single cell. The genes shown are differentially expressed between subtypes (log fold-change >0.1; $p<0.01$ from pairwise comparisons). (E) 3D reconstructions of an IHC and innervating nerve endings at P28. Upper panels: Cochlear whole mounts stained for TuJ1 (red; arrows) to identify type I SGNs projections and for CALB2 (green; arrowheads) to identify IHCs and type IA SGN projections. Lower panels: Whole mounts co-stained for CALB1 (green; arrows) and CALB2 (red; arrowheads). (F) 3D renderings (10 mice; 5–15 hair cells per sample) to quantify innervation patterns. We divided the base of IHCs into modiolar, middle and pillar side according to the TuJ1 innervation area and quantified the number of cells where $CALB2^+$ nerve fibers contacted IHCs. Values are mean ± SEM. Scale bar: 8μm.

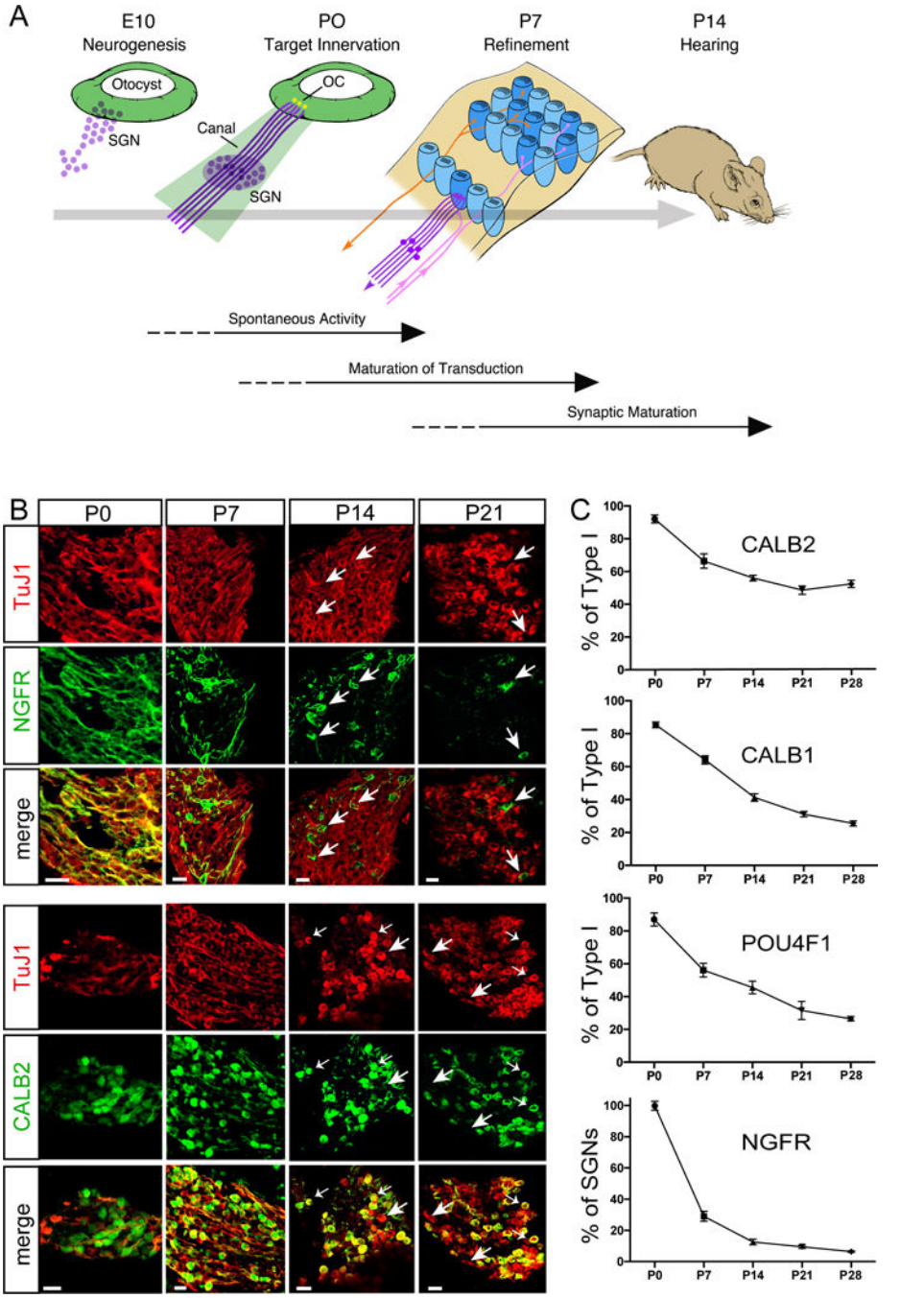

Fig. 4. Temporal specification of SGN subtypes.

(A) Diagram showing sequential steps during the maturation of the peripheral auditory sense organ. (B) Histological section through the spiral ganglion were stained with the indicated antibodies (large arrows: single-positive cells; small arrows: double-positive cells). (C) Quantification of the % of cells expressing different molecular markers at the indicated time points (serial sections from three mice at each time point; values are mean ± SEM). Scale bars: 20μm.

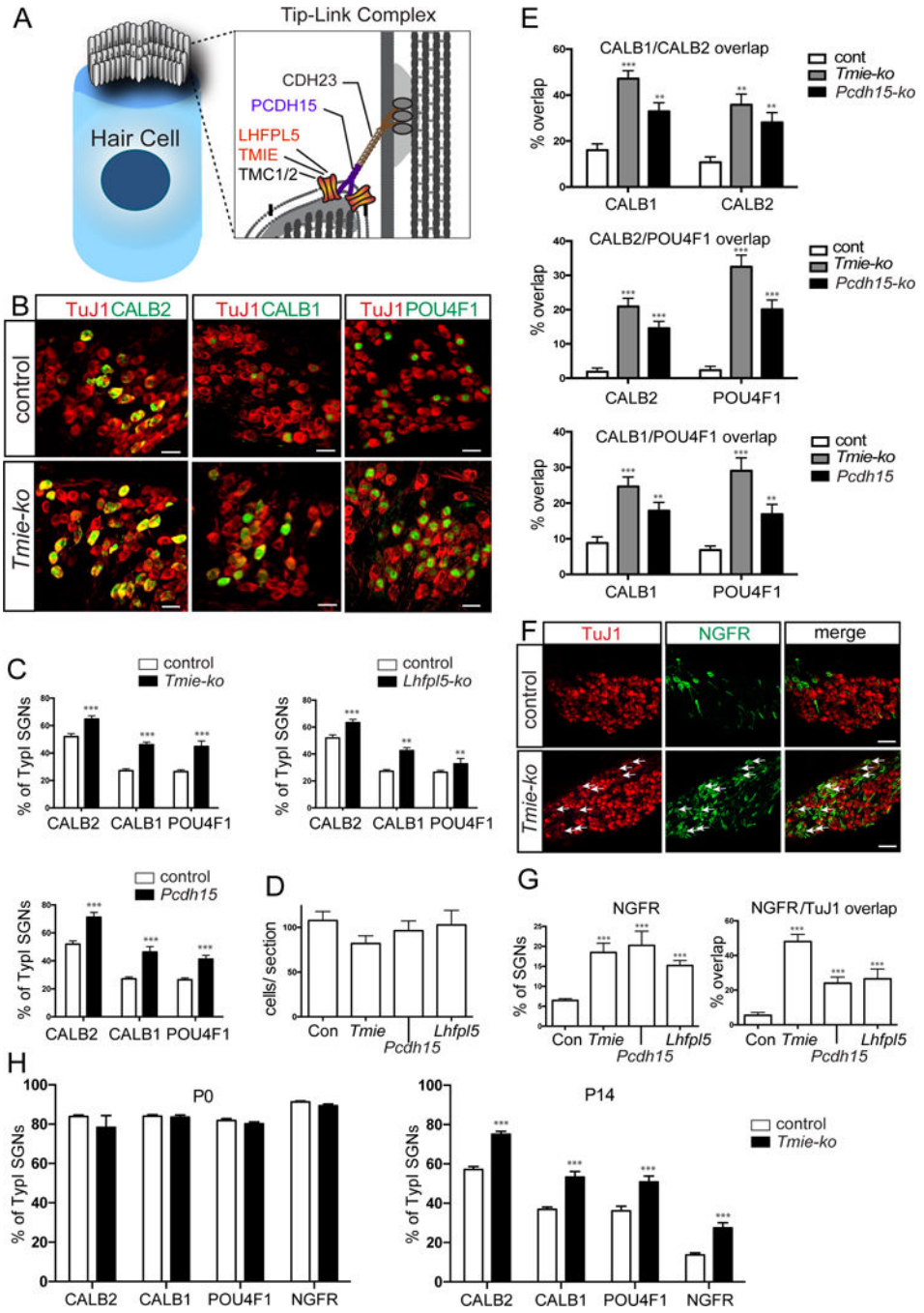

Fig. 5. Defects in hair cell mechanotransduction affects SGN subtype specification.

(A) Hair cell diagram. Inset: enlargement of the tip-link region indicating molecules of the mechanotransduction complex. (B) Sections through the spiral ganglion of control wild-type mice and *Tmie-ko* mice at P28 stained with the indicated antibodies. (C) Numbers of CALB2$^+$, CALB1$^+$ and POU4F1$^+$ SGNs in wild-type, *Tmie-ko, Lhfpl5-ko* and *Pcdh15-av3j* mice at P28. (D) SGN numbers at P28. (E) Numbers of CALB2$^+$, CALB1$^+$ and POU4F1$^+$ SGNs at P28. Total numbers of double positive cells were divided by numbers of cell expressing a single marker. (F) Histological sections of wild-type and *Tmie-ko* mice at P28

stained with the indicated antibodies (arrows: cells co-expressing TuJ1 and NGFR). (G) Numbers of $NGFR^+$ and $NGFR^+/TuJ1^+$ SGNs at P28. (H) Numbers of $CALB2^+$, $CALB1^+$, $POU4F1^+$ and $NGFR^+$ SGNs in mice of the indicated genotype at P0 and P14. For all experiments, serial sections from three animals of each genotype were analyzed. Values are mean ± SEM; two tailed unpaired t-test; *** $p<0.001$; ** $p<0.01$; * $p<0.05$. Scale bars: 20μm.

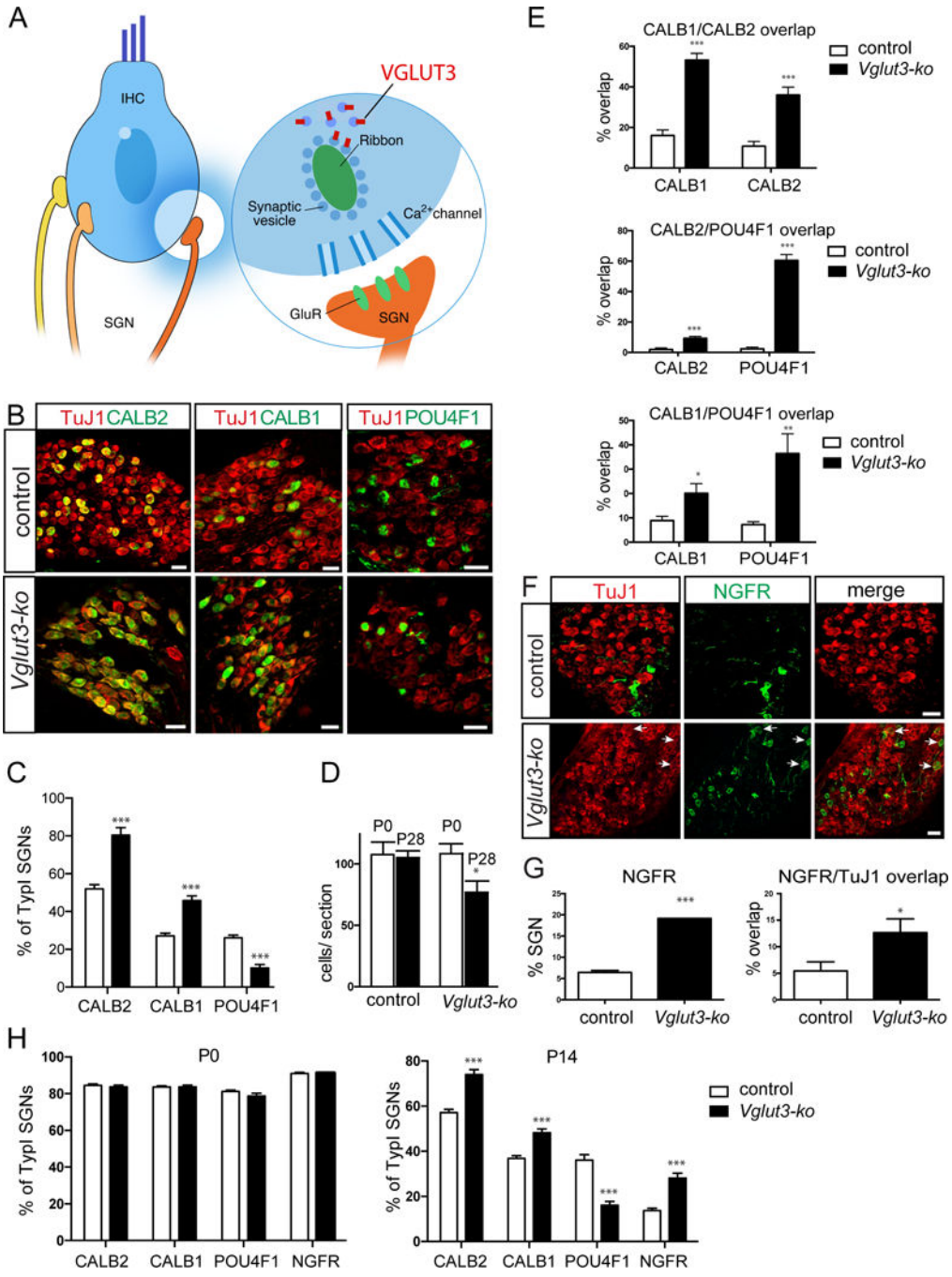

Fig. 6. Defects in glutamatergic signaling by IHCs affects SGN subtype specification.

(A) Diagram of an IHC with its innervating type I SGNs. Inset: enlargement of a ribbon synapse between IHCs and SGNs. Glutamate receptors (GluR) localizes to nerve terminals and VGLUT3 to synaptic vesicles. (B) Section through the spiral ganglion of control wild-type mice and *Vlgut3-ko* mice at P28 stained with the indicated antibodies. (C) Numbers of CALB2$^+$, CALB1$^+$ and POU4F1$^+$ SGNs in wild-type and mutants at P28. (D) SGN numbers at P28. (E) Numbers of CALB2$^+$, CALB1$^+$ and POU4F1$^+$ SGNs at P28. Total numbers of double positive cells were divided by numbers of cell expressing a single marker. (F)

Histological sections of wild-type and *Tmie-ko* mice at P28 stained with the indicated antibodies (G) Numbers of $Ngfr^+$ and $Ngfr^+/TuJ1^+$ SGNs at P28. (H) Numbers of $CALB2^+$, $CALB1^+$, $POU4F1^+$ and $Ngfr^+$ SGNs in mice of the indicated genotype at P0 and P14. For all experiments, serial sections from three animals of each genotype were analyzed. Values are mean ± SEM; two tailed unpaired t-test; *** $p<0.001$; ** $p<0.01$; * $p<0.05$.. Scale bars: 20μm.

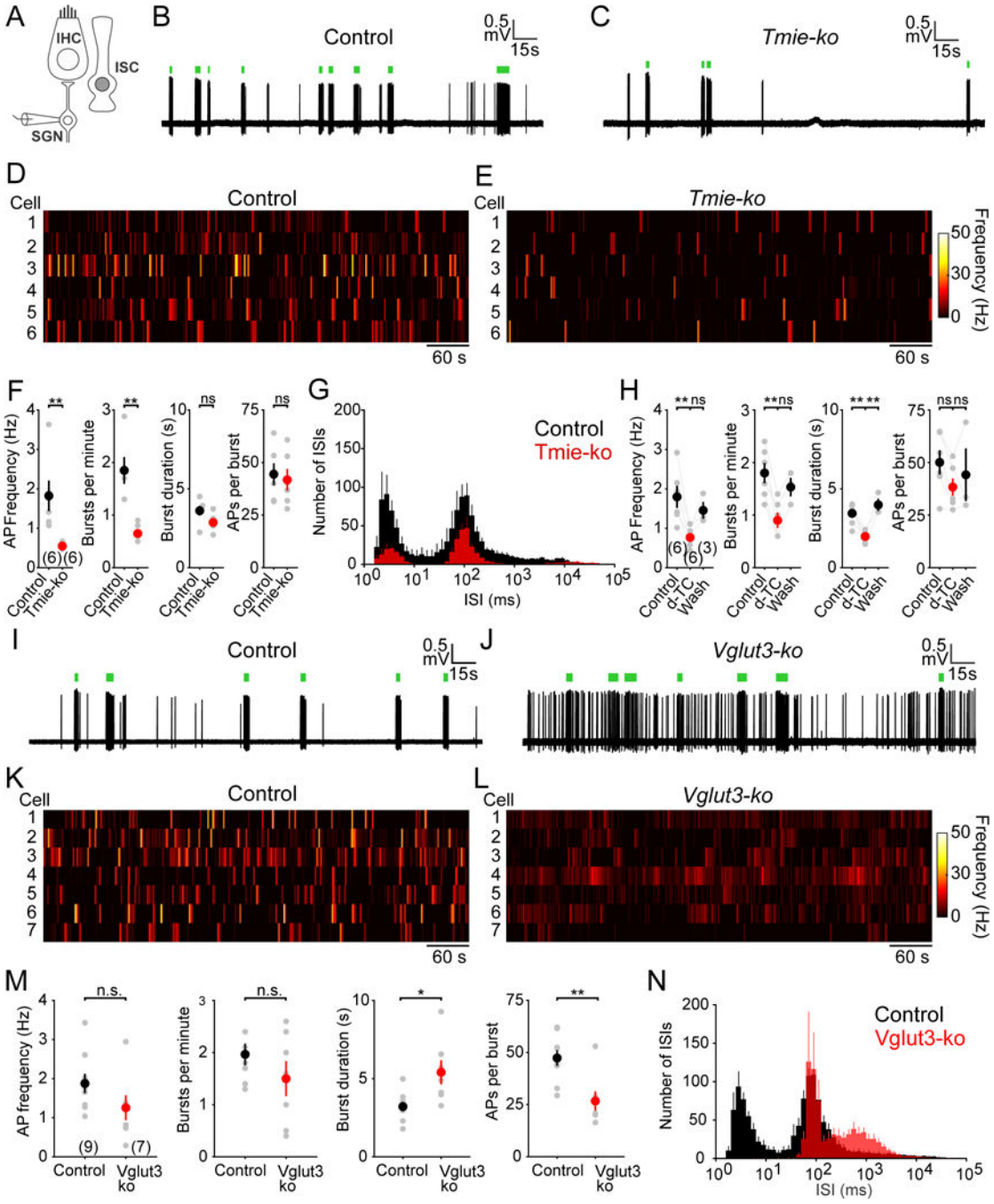

Figure 7. SGNs in *Tmie-ko* and *Vglut3-ko* mice exhibit altered burst firing before hearing onset.

(A) Diagram showing the juxtacellular recording configuration used to assess SGNs. ISC: inner supporting cell. (B, C) Spontaneous action potentials from SGNs in control (*Tmie*$^{+/+}$ or $^{+/-}$ littermates) and *Tmie-ko* mice. Green bars indicate discrete action potential bursts. (D, E) Raster plots indicating the average firing rate of SGNs (bin: 1 second) in control and *Tmie-ko* mice. (F) Quantification of average action potential (AP) frequency, frequency and duration of spontaneous bursts, and number of action potentials per burst from control and *Tmie-ko* mice. (G) Average log-binned interspike interval (ISI) histograms from control and

Tmie-ko mice. (H) Quantification of average action potential frequency, frequency and duration of spontaneous bursts, and number of action potentials per burst from cochleae treated with d-tubocurarine (d-TC; 50 μM). (I, J) Spontaneous action potentials recorded from SGNs of control (*Vglut3*$^{+/+}$ or $^{+/-}$ littermates) and *Vglut3-ko* mice. Green bars indicate discrete action potential bursts. (K, L) Raster plots indicating average SGN firing rates (bin: 1 second) in control and *Vglut3-ko* mice. (M) Quantification of average action potential frequency, frequency and duration of spontaneous bursts, and number of action potentials per burst in cochleae from control and *Vglut3-ko* mice. All values are mean ± SEM. Statistical significance calculated with two-tailed paired t-test, Bonferroni correction applied; ** $p<0.01$, * $p<0.05$, ns: not significant. (M) Average log-binned interspike interval (ISI) histograms from control and *Vglut3-ko* mice.